



Handcrafted Histological Transformer (H2T): Unsupervised representation of whole slide images

Quoc Dang Vu ^a, Kashif Rajpoot ^b, Shan E. Ahmed Raza ^a, Nasir Rajpoot ^{a,c,d,*}

^a Tissue Image Analytics Centre, Department of Computer Science, University of Warwick, UK

^b School of Computer Science, University of Birmingham, UK

^c The Alan Turing Institute, London, UK

^d Department of Pathology, University Hospitals Coventry & Warwickshire, UK



ARTICLE INFO

Dataset link: <https://github.com/vqdang/H2T>

Keywords:

Computational pathology
Unsupervised learning
Deep learning
WSI representation
Transformer

ABSTRACT

Diagnostic, prognostic and therapeutic decision-making of cancer in pathology clinics can now be carried out based on analysis of multi-gigapixel tissue images, also known as whole-slide images (WSIs). Recently, deep convolutional neural networks (CNNs) have been proposed to derive unsupervised WSI representations; these are attractive as they rely less on expert annotation which is cumbersome. However, a major trade-off is that higher predictive power generally comes at the cost of interpretability, posing a challenge to their clinical use where transparency in decision-making is generally expected. To address this challenge, we present a handcrafted framework based on deep CNN for constructing holistic WSI-level representations. Building on recent findings about the internal working of the Transformer in the domain of natural language processing, we break down its processes and *handcraft* them into a more transparent framework that we term as the Handcrafted Histological Transformer or H2T. Based on our experiments involving various datasets consisting of a total of 10,042 WSIs, the results demonstrate that H2T based holistic WSI-level representations offer competitive performance compared to recent state-of-the-art methods and can be readily utilized for various downstream analysis tasks. Finally, our results demonstrate that the H2T framework can be up to 14 times faster than the Transformer models.

1. Introduction

Visual assessment of tissue specimens under the microscope remains the *gold standard* for diagnosis of cancer and used for the purposes of prognostication and therapeutic planning (Gurcan et al., 2009; Abels et al., 2019). With the advancement in digitization, current pathology workflows increasingly use multi-gigapixel tissue images, now commonly known as whole slide images (WSIs), in a wide range of settings. These WSIs also enable pathologists to view the tissue samples remotely. Computational analysis of WSIs offers the promise for the detection of known diseases and, perhaps, the discovery of new disease subtypes.

In recent years, several machine learning approaches have been proposed for identifying nuclei, glandular structures or tumor-rich regions in histology images (Graham et al., 2019, 2020; Verma et al., 2021; Kather et al., 2019). There are currently two major approaches for WSI-level analysis. The first one is to construct features based on classification, detection or segmentation of the tissue components. These features are typically designed based on our knowledge from biological findings (Gentles et al., 2015), such as the co-localization of

lymphocytes surrounding cancerous epithelium (Shaban et al., 2019) or the deformation of glands in colon samples (Awan et al., 2017). Despite their effectiveness in prognosis and providing interpretability, there are several drawbacks during the construction of such pipelines. First and foremost, they rely mostly on annotated samples which are often intensive in terms of expert pathologists' time and effort (Amgad et al., 2019; Kromp et al., 2020). In addition, the pathologists are well-known to have high discordance on how a tissue sample or its constituents are labeled (Azam et al., 2021; Wahab et al., 2021).

In contrast, recent approaches have focused more on improving the discriminative power of the features (Lu et al., 2021; Li et al., 2021) rather than on the mechanism to derive a generic representation at the WSI-level. Although these approaches have achieved promising results, as with most deep learning based methods, they lack transparency and interpretability for their predictions. To mitigate this, recent techniques have utilized the attention mechanism to output a heatmap to indicate which instances the models rely on for making predictions (Ilse et al., 2018; Lu et al., 2021).

* Correspondence to: Department of Computer Science, University of Warwick, UK.

E-mail address: n.m.rajpoot@warwick.ac.uk (N. Rajpoot).

In this paper, we propose a novel way to obtain unsupervised holistic WSI-level representations based on a set of data-driven histological patterns, which we term as the *histological prototypical patterns*. The proposed representations, which we term as the handcrafted histological transformer (H2T) representations, are inspired by the attention mechanism of the well-known Transformers in natural language processing (NLP) (Vaswani et al., 2017) and attempt to model the attention mechanism in a handcrafted manner. We show that the proposed H2T representations are discriminative and can be readily utilized for various downstream analysis tasks with significantly reduced amount of effort. These representations are mined from the pixel data in WSIs and *handcrafted* from deep feature based representations or co-localization of histological pattern maps that commonly appear throughout the WSIs while indirectly incorporating the attention mechanism. Similar to the features constructed from tissue components which are considered to be highly interpretable, these patterns also facilitate tractability and interpretability of our derived WSI representations compared to other methods. We demonstrate that such interpretations can be achieved either through visual assessment or by retrieving closest image patches to the prototypical patterns. We evaluate the capacity of the derived prototypical patterns and the resulting H2T representations using two large publicly available WSI datasets: The Cancer Genome Atlas (TCGA) and Clinical Proteomic Tumour Analysis Consortium (CPTAC).

The main contributions of this work are as follows:

- We present a novel paradigm, termed as the handcrafted histological transformer (H2T), for deriving holistic WSI-level representations;
- We show how the proposed H2T representations can be constructed from histological prototypical patterns that are mined from WSIs in an unsupervised manner; in addition, we show how the prototypical patterns can be interpreted biologically and later utilized for discovery purposes;
- We provide a baseline Transformer model for WSI-level analysis, the first of its kind to the best of our knowledge;
- We show that the H2T representations are as predictive as the recent state-of-the-art methods (including the aforementioned Transformer model) while being computationally much cheaper, based on results from experiments on 6 datasets consisting of a total of 10,042 WSIs.
- We provide the code and the intermediate data (deep features and associated patterns) at <https://github.com/vqdang/H2T> to facilitate future investigation efforts.

2. Related work

2.1. Handcrafting representations for cytology and histology images

From the clinical and biological findings thus far, the morphology and distribution of tissue components such as gland or nuclei are recognized as strong indicators for cancer patient survival (Elston and Ellis, 1991; Goldstraw et al., 2016; Gentles et al., 2015). In lung tissue for instance, micropapillary and solid pattern are related to cancer with high degree of aggressiveness (Solis et al., 2012; Cao et al., 2016).

Early automated systems attempted to utilize the above information to differentiate tumor from normal tissue images. Hamilton et al. (1994) proposed a Bayesian network using the amount of nuclei, nuclear size, mucinous area, etc. quantified by cytologists as features for prediction. Keenan et al. (2000) developed a primitive automated nuclei detection method and then employed Delaunay triangulation to characterize the spatial distribution of detected nuclei. In their work, the resulting statistics of edges, vertices and triangles were features for predicting cervical intraepithelial neoplasia.

With the increase in compute power, automated methods which were previously restricted to just small images were then extended to

tissue microarray (TMAs) and WSIs. Tabesh et al. (2007), Kwak and Hewitt (2017) utilized morphological and textural features obtained from image patches for stratifying tumor grades of TMA cores. On the other hand, (Sertel et al., 2009) utilized a multi-resolution approach and extracted textural features at all resolution levels and then utilized them for making and refining prediction on WSIs in a coarse-to-fine manner.

Nonetheless, even with deep learning, processing large images by and large is still achieved by breaking them down into smaller parts (i.e., patches). In Hou et al. (2016), the authors first employed convolutional neural networks (CNNs) to classify image patches. Later, they either utilized the resulting histogram or fused features from patches to make predictions for an entire WSI. Around the same time, new clinical findings indicated that a large number of lymphocytes infiltrating deep within the tumor sites carry prognostic significance (Shield et al., 2017). Shortly after, Shaban et al. (2019) proposed an automated method to obtain a single score to measure the amount of tumor-infiltrating lymphocytes (TILs) that is predictive of patient survival. This involves robustly identifying the tissue types of all image patches within a large cohort of WSIs. This form of analysis is taken further in later works. Diao et al. (2021) extracted multiple statistics of tissue components and demonstrated that these features still correlate well with recently established tumor microenvironment markers as well as molecular signatures.

2.2. Learning WSI representations

While handcrafted WSI features like the above remain a potent way to predict disease status (Amgad et al., 2019; Kromp et al., 2020), the methods for obtaining those representation are often laborious and time-consuming. To lessen the burden of annotation, the medical image processing analysis community turned to multiple instance learning (MIL) to predict the label of a bag of instances without needing to identify the labels of the constituent parts (or instances) (Dietterich et al., 1997; Andrews et al., 2002). In computational pathology, each instance is a feature vector of an image patch. These vectors are assumed to be highly compact while still being discriminative enough for major tissue patterns. Due to this assumption and heavy reliance on deep feature representation of a patch, a majority of the techniques have focused more on improving the discriminative power of the features (Lu et al., 2021; Li et al., 2021; Kalra et al., 2021; Abbet et al., 2020). In particular, several methods applied weakly supervised learning while treating the WSIs as bags of instances (image patches) with respect to a specific task, such as classification of WSIs (Campanella et al., 2019; Bilal et al., 2021).

While such systems could allow us to do away with a large amount of human *a priori* knowledge, finding and attributing which instances are important to the prediction remains difficult (Kandemir and Hamprecht, 2015). Without being able to localize down to the instance-level, interpretation of the model could not be made for clinical settings. In order to resolve this, recent works like (Campanella et al., 2019) utilized visualization techniques to increase the interpretability of their results. Specifically, while they used a recurrent neural network (RNN) for prediction, they applied t-SNE (Van der Maaten and Hinton, 2008), a manifold mapping, on their input instances to extract their placements within the model decision space.

Recently, neural networks with attention mechanism came forth as a powerful tool for the medical image analysis community. In particular, they can not only learn a discriminative bag-level representation but also provide interpretable and relatable instance-level attributions (Ilse et al., 2018). In order to apply this method to WSI-level analysis, WSIs are commonly split into patches where each is passed through a pretrained CNN for feature extraction. The resulting set of feature vectors is then input to a proposed neural network for training and making predictions (Lu et al., 2021; Li et al., 2021; Kalra et al., 2021; Hashimoto et al., 2020) while each image patch is considered as an

instance in the MIL setting. Because the patch-level representation is the most critical building-block for these methods, many works focus on designing a scheme to enrich this representation. MS-DA-MIL (Hashimoto et al., 2020) employed adversarial training to enrich the instance-level features before inputting them into a multi-scale attention model. More recently, CLAM (Lu et al., 2021) utilized a loss to pull the representation of patches within a specific label closer together. DSMIL-LC (Li et al., 2021) proposed using SimCLR (Chen et al., 2020) (self-supervised contrastive learning) to derive patch-level representations and a scheme to combine instance-level prediction with bag-level prediction. FocAtt-MIL (Kalra et al., 2021) refined the patch-level features by training the feature extractor with hierarchy of instance labels.

Concurrent to the above developments, natural language processing (NLP) recently experienced tremendous breakthrough via the adoption of Transformer models (Vaswani et al., 2017) which were pretrained on large NLP datasets such as GPT-3 (Brown et al., 2020). Although Transformer is also an attention-based neural network at its core, we consider it as a more generalized form of attention mechanism compared to the methods mentioned previously. Since its inception, Transformers have been adopted by other fields with great success. For instance, using a Transformer-based architecture, AlphaFold achieved a significant improvement compared to all other methods on a 50 years old grand challenge (Jumper et al., 2021) in predicting the protein folding structure. In natural image analysis, Vision Transformers have achieved comparable performance against ResNet (Dosovitskiy et al., 2020). Furthermore, in some cases, Transformer-based networks have shown to be more robust than CNNs (Hendrycks et al., 2021). In computational pathology, Myronenko et al. (2021) have recently adopted Transformer for predicting Gleason grades of WSIs.

2.3. Transformers and context-based image retrieval

Recent theoretical analysis and empirical evidence on Transformer families (i.e., those utilizing multi-head self-attention mechanism) have demonstrated that they have strong capability for retrieving information (Chen et al., 2022b). Specifically, the theoretical analysis by Ramsauer et al. (2020) showed that MHA can directly use raw images for querying and/or storing other raw images (i.e. acting like code books in term of dictionary learning) without any training. On the other hand, Tan et al. (2021) and Mari et al. (2022) extended the Transformer architecture so that it can extract more efficient descriptors for image retrieval problems.

With these evidence, we consider Transformer as one of the most powerful context-based image retrieval (CBIR) techniques in the current times for representing WSIs.

2.4. Unsupervised learning

Traditionally, unsupervised learning methods are defined as techniques that do not rely on labels to obtain the data underlying representation. Prime examples include clustering methods and other traditional dimensionality reduction techniques like Principal Component Analysis, k-means clustering, UMAP (McInnes et al., 2018) or t-SNE (Van der Maaten and Hinton, 2008). However, in the current literature, by relaxing the definition of “no label” to “**no human supervisory signals**” (Dörsch and Zisserman, 2017), unsupervised learning can be framed as self-supervised learning. Thus, self-supervised learning is a subset of unsupervised learning where the guidance signals for the training process can be obtained by directly interacting with the data itself. Typical self-supervised learning supervisory signals include filling in image holes, solving jigsaw puzzles made from image patches, predicting movement in videos or more (Kim et al., 2019; Chen et al., 2020). Empirically, relaxing the conditions about the label origins have led to the discoveries of much more general and robust representations (Caron et al., 2020; Chen et al., 2020).

In relation to H2T, while our proposed framework’s performance relies on the deep features, which can be obtained either by self-supervised learning or supervised learning, its internal mechanism consists of only clustering methods and operations that do not rely on any human labels. Thus, we consider that our proposed framework fits well in the traditional category of unsupervised learning as described previously.

2.5. Representation of image patches

Several applications, not limited to medical image processing, have utilized CNNs pretrained on ImageNet in a supervised manner for various different tasks. However, recent advancements in computer vision have again emphasized the importance of obtaining a strong representation. In particular, Hendrycks et al. (2019), Djolonga et al. (2021), Koohbanani et al. (2021) have demonstrated that representations derived from self-supervised learning are more robust than those obtained solely from supervised learning. Many recently proposed techniques like SimCLR (Chen et al., 2020) are also rapidly closing the gap between self-supervised learning and supervised learning. In particular, SWAV (Caron et al., 2020) surpassed the performance of ResNets which were trained on ImageNet in a supervised manner. In computational pathology, Giga et al. (2020) recently assessed SimCLR on a large cohort and showed that self-supervised training small CNNs on histopathology images is more beneficial for downstream tasks compared to those pretrained on ImageNet with supervised learning.

3. Methodology

Recent automated methods not only require much less human annotation but also can be more predictive compared to their more traditional counterparts. However, as a trade-off for their improvement in predictive power, their internal processes are difficult to interpret to human operators. Moreover, their computational cost can sometimes be prohibitively expensive. Herein, we propose a method that is more interpretable and computationally cheaper without compromising on predictive power.

3.1. Handcrafted histological transformer (H2T)

Inspired by the Transformer and the recent works that unravel its mechanism, we breakdown Transformer operation and re-construct them in a handcrafted manner for histology-related tasks. We refer to the proposed framework as Handcrafted Histological Transformer (H2T). As shown in Fig. 1, there are two stages of the H2T for representation learning:

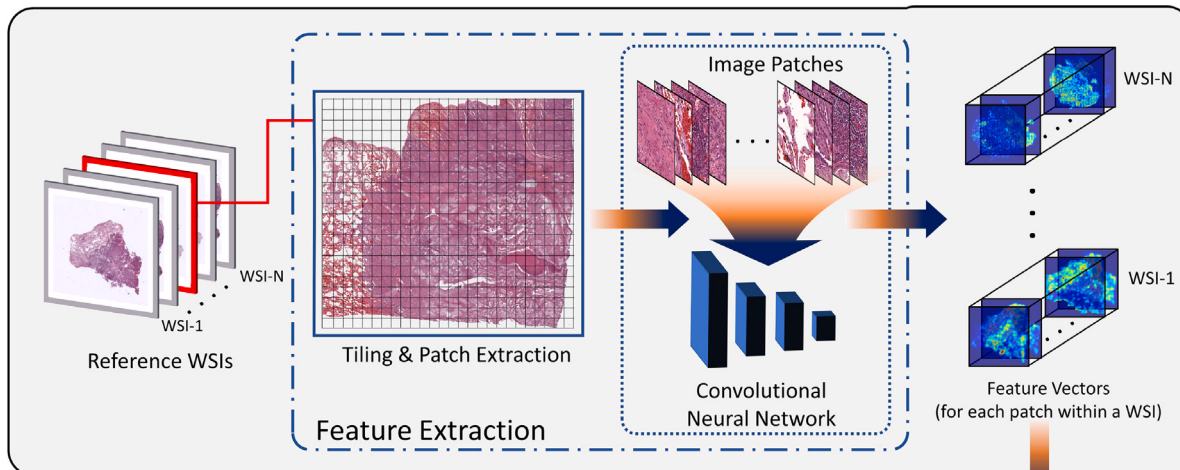
- a. Construction of the prototypical patterns;
- b. Projection against these patterns.

In the first stage, we extract a set of prototypical patterns from a set of *reference* WSIs (later referred to as the reference cohort). In order to obtain the most representative patterns, it is crucial to utilize a large enough and representative repository of WSIs from multiple sources. In the second stage, new WSIs are projected against the prototypical patterns and are summarized based on the relationship between their constituent instances and their assigned patterns. In the final stage, we utilize the resulting representation of WSIs for subsequent analysis.

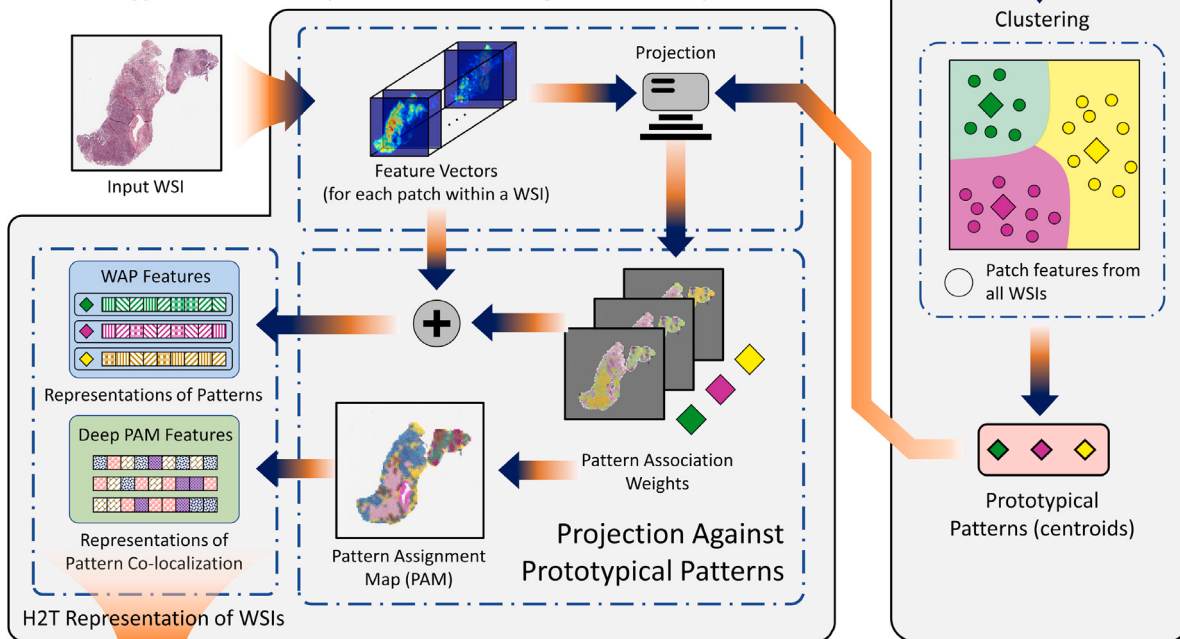
We demonstrate that the resulting representations are highly discriminative and can be readily used with relative ease. Owing to the relatively low computational requirements, the predictive power of their representations and many unsupervised steps within, we show that the proposed framework can also be used for data discovery purposes such as out of distribution detection.

In the remainder of this section, we first describe the key mechanism behind the Transformer attention. We then describe in depth how H2T representations are formulated in a similar fashion but without employing an explicit attention module.

A. Unsupervised Prototypical Pattern Extraction



B. Prototypical Pattern Projection / Generating WSI-level Representation



C. Downstream Analysis

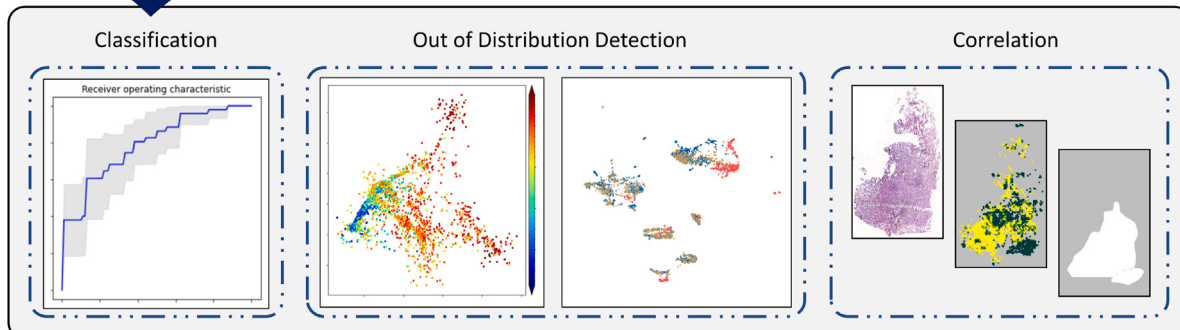


Fig. 1. Our proposed Handcrafted Histological Transformer (H2T) framework. The framework revolves around the extraction and the utilization of the prototypical patterns. By projecting a new WSI against this set of prototypical patterns, we derive highly discriminative WSI representations that are readily usable for other downstream tasks. In the feature vector images (the stacks of blue images), each pixel corresponds to a patch in the WSI and the depth corresponds to the features from a CNN. Throughout the framework, these features are extracted using the same pretrained CNN. In our case, this can either be from ResNet50 pretrained on ImageNet or ResNet50 pretrained by SWAV self-supervised learning method (Caron et al., 2020). The Pattern Association Weights are described in Eq. (6).

3.2. Multi head self-attention

The multi head (self) attention (MHA or MHSA) architecture and its powerful modeling capacity was popularized via the Transformer architecture (Vaswani et al., 2017). The core of the Transformer, or the MHA to be exact, is centered around the following formulation:

$$\begin{aligned}\hat{Q} &= \text{softmax} \left(\frac{1}{\sqrt{d_k}} Q K^T \right) V \\ &= \text{softmax} \left(\frac{1}{\sqrt{d_k}} Q W_Q W_K^T K^T \right) V W_V\end{aligned}\quad (1)$$

Here, \hat{Q} is the attention output of a single head while K , Q and V are commonly referred to as the key, query and value inputs. We denote the associated dimensions of their features as d_k , d_q and d_v . Additionally, $W_K \in \mathbb{R}^{d_k \times d_e}$, $W_Q \in \mathbb{R}^{d_q \times d_e}$ and $W_V \in \mathbb{R}^{d_v \times d_e}$ are learnable weights for projecting each input feature into a common space with dimensionality d_e .

By constructing multiple such modules and selecting features within \hat{Q} from each head h together, we obtain the renowned MHA architecture:

$$\text{MultiHeadAttention}(Q, K, V) = \text{Concat}(\hat{Q}_1, \dots, \hat{Q}_h) W_L \quad (2)$$

where h is the total number of heads and the projection weight matrix $W_L \in \mathbb{R}^{hd_e \times d_v}$ is learnable.

According to Ramsauer et al. (2020), by using the same input Y for K and V and by renaming the input Q as R , Eq. (1) can take the form:

$$\begin{aligned}\hat{Q} &= \text{softmax} \left(\frac{1}{\sqrt{d_k}} Q W_Q W_K^T K^T \right) V W_V \\ &= \text{softmax} \left(\beta R W_Q W_K^T Y^T \right) Y W_V\end{aligned}\quad (3)$$

where β is a scaling factor.

Under the above formulation, Ramsauer et al. (2020) proved that MHA is closely related to Hopfield neural network. Additionally, they identified several interesting properties. First of all, the above equation is synonymous with finding the association between inputs R and Y , using R as reference. Secondly, the scaling factor $\beta = \sqrt{1/d_k}$ is of particular importance as it controls the degree of memorization and association capacity of the architecture. Finally, if we take a step further and consider that R is trainable, we effectively obtain an architecture that learns a set P of prototypical patterns from the training set. Accordingly, this is synonymous to letting the network learn how all instances within the input are related to a prototypical pattern p . Once the set of patterns are identified, the network then performs weighted average pooling over input instances to derive a representation of the input sequence. Furthermore, by stacking multiple attention heads, it becomes possible for the network to derive multiple prototypical patterns.

3.3. Positional encoding

Another component that is often used together with MHA is the positional encoding. It is apparent from Eq. (1) that MHA is permutation invariant with respect to the ordering (or position) of input instances. As such, in cases where positions are of extreme importance, it is crucial for us to incorporate this information within the network design. At the moment, this is commonly achieved via sine-encoding (or Fourier-encoding) where they are either added or concatenated together with the instance features. In computer vision, using positional encoding makes a significant difference in performance for methods using MHA within their solution (Carion et al., 2020).

With d_ψ as the number of features (or embedding dimensions) within the vector representing the image patch (or instance), for 2D dimensions with x and y respectively as the instance positions along the x and y axes within the WSI, we use the following position encoding

function (PE) to encode the position of each instance ψ for a given embedding dimension j :

$$\begin{aligned}PE(x, y, j) &= \text{Concat}(PE_{\sin}(x, 4j), PE_{\cos}(x, 4j + 1), \\ &\quad PE_{\sin}(y, 4j + 2), PE_{\cos}(y, 4j + 3))\end{aligned}\quad (4)$$

$$\begin{aligned}PE_{\sin}(x, 4j) &= \sin \left(\frac{x}{e^{4j/d_\psi}} \right) \\ PE_{\cos}(x, 4j + 1) &= \cos \left(\frac{x}{e^{(4j+1)/d_\psi}} \right) \\ PE_{\sin}(y, 4j + 2) &= \sin \left(\frac{y}{e^{(4j+2)/d_\psi}} \right) \\ PE_{\cos}(y, 4j + 3) &= \cos \left(\frac{y}{e^{(4j+3)/d_\psi}} \right)\end{aligned}\quad (5)$$

Here, $e = 10000$ is the assumed maximum value of x and y along the corresponding axes within the WSI. From the above equation, there are four components derived for a given embedded dimension j . In order to ensure that the resulting positional encoding vector maintains the same dimensionality as the feature vector ψ , we further define $j \in \{0, \dots, d_\psi/4\}$.

In our case, while the width and height of a WSI can reach hundred thousands pixels, in practice, we can normalize the patch locations into relative positioning. For example, by extracting patches of size 512×512 and stride of 512×512 from a WSI of 51200×51200 , we can effectively denote each patch belonging to a 100×100 canvas. The x and y positions of each image patch are thus ensured to be smaller than the e limit defined in Eq. (4).

3.4. Handcrafted prototypical patterns

Recently, features based on co-localization of specific nuclei types such as TILs have been shown to be robust and prognostic (Shaban et al., 2019). In addition, there is recent evidence to suggest that morphology of tissue components can also be predictive (Diao et al., 2021).

Given the formulation in Eq. (1), the importance of encoding positional information and the successes so far of its less general variants on WSI prediction tasks, we first assume that the resulting representation vector from MHA is highly discriminative. In addition, it also contains information on the variation within instance features (or instance-level patterns) and how these variations co-occur with each other (instance-level co-localization patterns). Under this formulation, H2T representation of WSIs offers the following:

- We can disentangle the features related to instance-level patterns from those for co-localization of patterns;
- Instead of learning prototypical patterns in a supervised manner, as in some of the recent works, we can provide our own set of reference patterns;
- Rather than learning the attribution of each instance for composing the WSI representation, we can derive an effective attribution ourselves;
- Similarly, we can also devise the co-localization in a handcrafted manner.

Going forward, we use instance ψ to denote an image patch's feature vector within a WSI. This image patch can be of arbitrary size and from an arbitrary magnification level.

3.4.1. Representations from histological patterns

Prototypical patterns of a set of image patches (or strictly speaking, their feature vectors) can be obtained via clustering. While there are many clustering techniques, not many of them scale well when processing millions of input samples, as in our case. Therefore, given the large amount of image patches and the high-dimensionality of their feature vectors, we use k -means clustering. Utilization of k -means and nearest

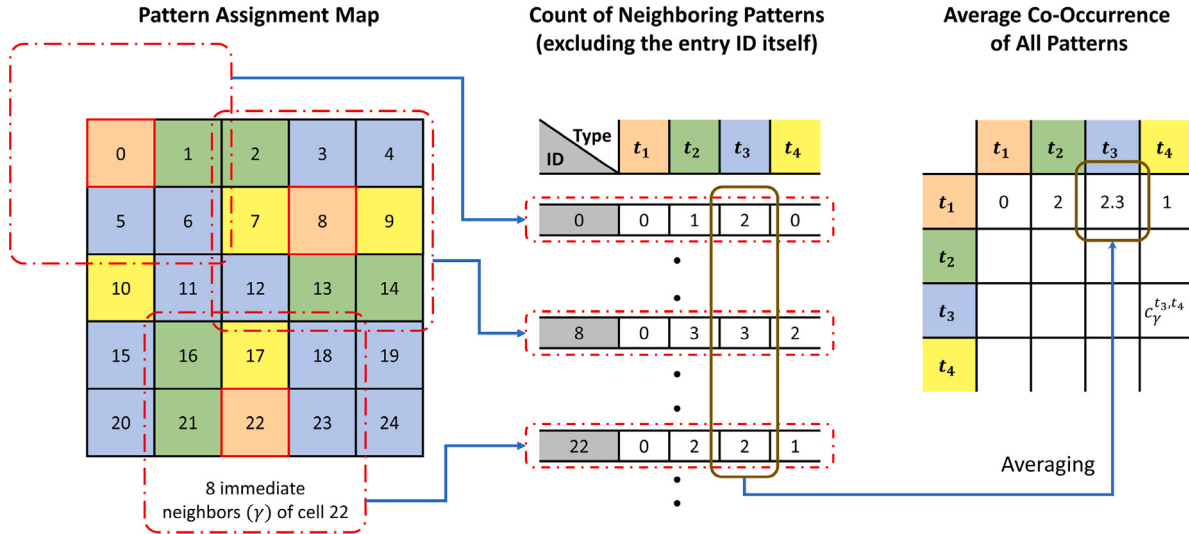


Fig. 2. Step by step illustration of how 8 is utilized to calculate the pattern co-localization matrix (PCM). Here, each pattern (or type t_k) is denoted in a different color. It is worth noting that the pattern counting does not include the type of entry (or the central) cell.

neighbors has been noted to be particularly effective for tasks on the same magnitude of difficulties (Wang et al., 2019). For this usage, it is crucial to normalize the feature vector of each image patch with L_2 -norm.

As a result, the (prototypical) histological patterns $p \in P$ are also the resulting centroids obtained from the clustering process. With ψ denoting the feature vector of an image patch, we therefore reformulate Eq. (3) into the following form,

$$\overline{H}_i = \frac{1}{|\Phi_i|} \sum_{\forall \psi_j \in \Phi_i} f(p_i, \psi_j) \odot \psi_j \quad (6)$$

$$\overline{H} = \text{Concat}(\overline{H}_0, \dots, \overline{H}_N) \quad (7)$$

where \overline{H}_i is representation when projecting the WSI against the i th prototypical histological pattern p_i and Φ_i is the set of image patches assigned to p_i . Specifically, a patch ψ is assigned to a pattern p_i when the distance between their representations is the smallest compared to all other patterns. In Eq. (6), $f(p_i, \psi_j)$ is an attribution function that measures the similarity between p_i and ψ_j and \odot denotes the element-wise multiplication of two vectors. The resulting \overline{H} is, therefore, the WSI representation when projected against a derived set of histological prototypical patterns P . We refer to \overline{H} as weighted average pooling (WAP) features in Fig. 1.

There are several ways to derive the attribution of each instance ψ (image patch) with respect to their assigned prototypical pattern p_i . Assuming that both p_i and ψ_j have already been normalized by L_2 -norm and $d(p_i, \psi_j)$ is their Euclidean distance, we investigate the following attribution function $f(p_i, \psi_j)$:

1. \overline{H} : Average pooling of all assigned ψ_j , we effectively set $f(p_i, \psi_j) = 1$ in this scenario.
2. $\overline{H}\text{-w}$: Weighted pooling of the assigned ψ_j . Here, the weights are the inverse distance between p_i and its ψ_j . Thus, we define $f(p_i, \psi_j) = 1 - d(p_i, \psi_j)$.
3. $\overline{H}\text{-t}[X]$: Similar to #1, with Φ_i further filtered such that only patches having $d(p_i, \psi_j) \geq X$ are selected for aggregation.
4. $\overline{H}\text{-k}[X]$: Similar to #1, with Φ_i further filtered such that only top X instances that are the **closest** to p_i are selected for aggregation.
5. $\overline{H}\text{-fk}[X]$: Similar to #1, with Φ_i further filtered such that only top X -th instances that are the **furthest** to p_i are selected for aggregation.

3.4.2. Representations from co-localization of patterns

Inspired by how features describing co-localization of different nuclei types can be constructed (Abbet et al., 2020), we define the pattern co-localization matrix (PCM) as follows,

$$\begin{aligned} c_{\gamma}^{i,j} &= \frac{1}{|\Phi_{\gamma}^{i,j}|} \sum_{\psi \in \Phi_{\gamma}^{i,j}} u_{\gamma}^{i,j} \\ \widehat{C}(\gamma) &= \begin{bmatrix} c_{\gamma}^{1,1} & \cdots & c_{\gamma}^{1,j} \\ \vdots & \ddots & \vdots \\ c_{\gamma}^{i,1} & \cdots & c_{\gamma}^{i,j} \end{bmatrix} \end{aligned} \quad (8)$$

where $\Phi_{\gamma}^{i,j}$ is a set of patches where each instance not only belongs to pattern p_i but is also surrounded by patches of pattern p_j within the radius γ . We additionally denote $u_{\gamma}^{i,j}$ as the number of patches assigned to pattern p_j within the neighborhood of patch $\psi \in \Phi_{\gamma}^{i,j}$. With these definitions, $c_{\gamma}^{i,j}$ can be understood as the average occurrence of pattern p_j around pattern p_i within the distance γ . Meanwhile, $\widehat{C}(\gamma)$ is the average pattern co-localization (PCM) matrix of all patterns within the WSI. Finally, we only study the 8 immediate neighbors in this paper. This calculation is illustrated in Fig. 2.

While we can extend the number of γ for assessment and stack many resulting $\widehat{C}(\gamma)$ together for a more detailed representation, they still only reflect one aspect of the co-localization distribution, which is their mean. It would become unscalable when trying to incorporate longer distance and/or other distribution measurements.

To resolve this issue, we can employ CNNs (or graph neural networks for a more general form) to learn the patterns of co-occurrence. Specifically, with a set of patches Φ_i assigned to each pattern p_i from Eq. (6), because we know the position of each patch within the original WSI, we can therefore project such assignments back to their 2D relative positioning. By repeating this process for all prototypical patterns, we obtain an image which we denote as the Pattern Assignment Map (PAM). It is worth noting that this projection is akin to a coarse segmentation process i.e. patch-wise classification rather than pixel-wise classification. It is expected that a neural network trained on this image can therefore learn the patterns of co-occurrence.

In the case of using CNNs, the prototypical PAM is not the same as a normal image where each pixel value is a category rather than the raw pixel intensity. We are therefore encouraged to encode and train the CNNs on such encoding rather than learning the PAM directly. For categorical values like ours, one-hot encoding is an exceptionally cheap and effective way for such modeling. To differentiate with the hand-crafted co-occurrence features from 8, we term the features obtained from training CNNs as Deep PAM features and denote them as \overline{C} .

Table 1

Summary of the main datasets used in our experiments. It is worth noting that the Normal WSIs utilized here are adjacent to the Tumor WSIs within the biopsy samples. Additionally, TCGA-Lung (NSCLC) is a combination of tumorous WSIs within TCGA-LUAD and TCGA-LUSC dataset.

Datasets	Tissue type/Organ	FFPE WSIs	Frozen WSIs	Total WSIs	Total patients
CPTAC-LUAD	Lung	0	1048	1048	111
	Normal	0	374	374	–
	Tumor (Adenocarcinoma)	0	674	674	–
CPTAC-LUSC	Lung	0	1025	1025	108
	Normal	0	363	363	–
	Tumor (Squamous Cell Carcinoma)	0	662	662	–
TCGA-LUAD	Lung	531	1067	1598	522
	Normal	0	244	244	–
	Tumor (Adenocarcinoma)	531	823	1354	–
TCGA-LUSC	Lung	512	1200	1712	504
	Normal	0	347	347	–
	Tumor (Squamous Cell Carcinoma)	512	853	1365	–
TCGA-Lung (NSCLC)	Lung — Non-Small Cell Carcinoma	1043	1676	2719	1026
	Adenocarcinoma	531	823	1354	522
	Squamous Cell Carcinoma	0	662	662	504
TCGA-Breast (BRCA)	Breast — Carcinoma	992	1317	2309	975
	Invasive Ductal	791	1090	1881	776
	Lobular	201	227	428	199
TCGA-Kidney (RCC)	Kidney — Renal Cell Carcinoma	909	1441	2350	926
	Clear Cell	504	1062	1566	523
	Papillary Cell	296	236	532	290
	Chromophobe Cell	109	143	252	113
Total (Unique)	Lung, Breast, Kidney	2944	7098	10042	3048

4. Experimental results

4.1. Datasets

For this study, we utilized 6 different datasets consisting of a total of 10,042 *unique* WSIs from 3048 *unique* patients from The Cancer Genome Atlas (TCGA) and Clinical Proteomic Tumour Analysis Consortium (CPTAC). The number of WSIs and the distribution of associated labels within each dataset are summarized in [Table 1](#). We constructed TCGA-Lung (NSCLC) dataset by using only tumorous WSIs within TCGA-LUAD and TCGA-LUSC dataset.

For the same patient, in addition to the tissue slides that contain tumorous area, there are also normal adjacent tissue slides. Thus, for lung tissue, there are 3 WSI-levels: Normal, Lung Adenocarcinoma (LUAD) and Lung Squamous Cell Carcinoma (LUSC). For breast tissue, there are 2 WSI-level labels: Invasive Ductal (IDC) and Lobular Carcinoma (ILC). Lastly, for kidney, there are 3 WSI-level labels: Clear Cell, Papillary, and Chromophobe Renal Cell Carcinoma (CCRCC, PRCC, CHRCC). Although there are slides that may come from the same patient, for simplicity, in this study we treated each WSI as an independent sample.

Aside from the TCGA and CPTAC cohorts, we also utilized 2 WSIs from the ACDC ([Li et al., 2020](#)) dataset for rough qualitative assessment.

4.2. Evaluation

Our H2T framework is a handcrafted approximation of the inner working of the Transformer. Therefore, it is of interest to determine how closely H2T approximates the performance of the original Transformer architecture. In order to assess this, we specifically trained two Transformer models as baseline: transformer-1 with only one multi head attention (MHA) layer for the final aggregation; and transformer-2 with one multi head self-attention (MHSA) layer and one MHA layer for the final aggregation.

We linearly probe the discriminative power of our resulting WSI-level representation on a series of classification tasks. This is a widely utilized technique in the computer vision community for assessing feature representation obtained from self-supervised learning ([Chen et al., 2020](#); [Caron et al., 2020](#); [Zhang et al., 2016](#)). Specifically, the features

are considered to be usable only if they are highly discriminative out-of-the-box. In other words, the degree of their discriminative power is reflected by their linear-separability. In our case, the discriminative power of the resulting WSI-level H2T representations directly correlates with the usability of the prototypical patterns utilized to construct them. Finally, this probing is achieved by inputting the features through a single linear layer for making the prediction.

In subsequent experiments, we used either CPTAC or TCGA as the discovery set, namely being training and validation set. On the other hand, we kept the entire other cohort as evaluation set (independent testing set). Within the discovery set, we split the cohort across both labels and the subset (such as CPTAC-LUAD and CPTAC-LUSC) into 5 folds in a stratified manner. For each fold, we then selected the best model and validated it on the testing cohort. Subsequently, we reported the mean and standard deviation obtained from each fold from both the discovery and evaluation cohort.

We evaluate our representation on several classification tasks: Normal vs Tumor of lung tissue (LUAD and LUSC are combined to make Tumor label), LUAD vs LUSC, Normal vs LUAD vs LUSC of lung tissue, CCRCC vs PRCC vs CHRCC, or IDC vs ILC. To be in line with existing methods that have been applied for the Normal vs Tumor and cancer sub-typing tasks, we use area under the receiver operating characteristic (AUROC) as the evaluation metric. However, due to the skewed distribution of labels within the dataset, we additionally calculate average precision (AP), which is another way to compute the area under the precision-recall curve (AUPRC), for each label and report their mean (mAP).

Aside from assessing the predictive power of our proposed WSI-level representation, we are also interested in how prototypical patterns which originate from different source tissue (the reference cohort) would impact downstream analysis. In this study, we consider two scenarios: tissue coming from different centers and/or different tissue types. Throughout the main text, we focus on the first scenario: using all available tissue within TCGA or CPTAC when one of them is the discovery cohort. For example, with LUAD vs LUSC, when TCGA is used as the discovery cohort, all prototypical patterns are extracted using *only* TCGA data whereas CPTAC data are kept intact as independent testing set. On the other hand, the Supplementary Material explores the latter case: using *only* Normal tissue within TCGA or CPTAC when one of them is the discovery cohort.

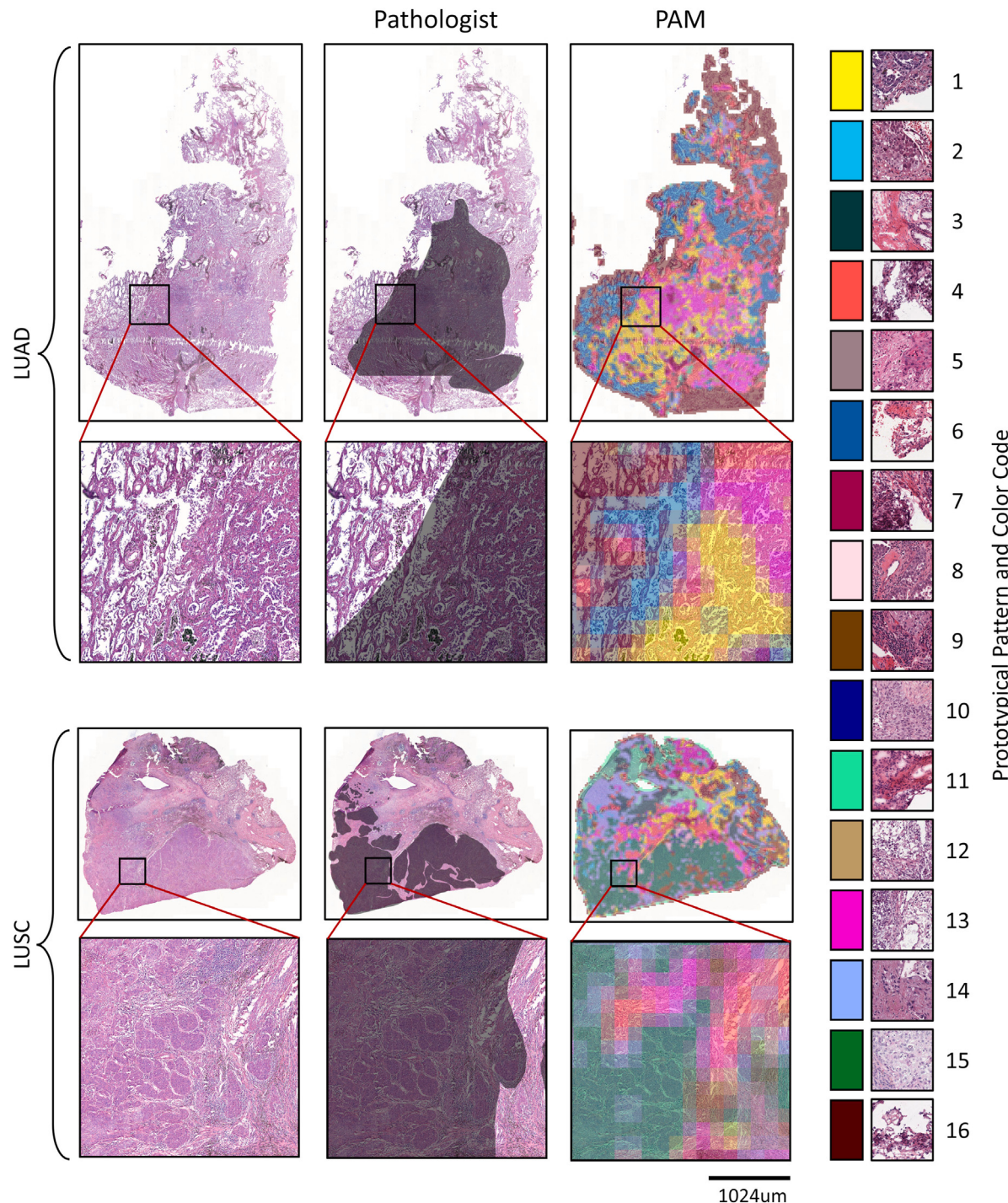


Fig. 3. Comparison of pattern assignment maps (PAMs) against the annotations from the pathologists on lung tissue. PAMs were constructed using 16 prototypical patterns. By using SWAV-ResNet50 patch-level features, these patterns were derived from all WSIs within the TCGA cohort. The sample WSIs in the figure are from ACDC cohort and the overlaid areas with dark shade are tumorous regions provided by pathologists. We visually identify that prototypical patterns with ocean blue color (6) or deep red color (16) are closely related to Normal tissue areas; patterns with yellow (1) or pink (13) colors are related to tumorous area in LUAD; and pattern with green color (15) is related to LUSC. When selecting out areas having these tumorous patterns and quantitative measuring them against the pathologist annotations, we obtained 0.6879 ($p < 0.0001$) and 0.8407 ($p < 0.0001$) in Pearson correlation coefficient for LUAD and LUSC respectively. The same set of prototypical patterns were later utilized for Fig. 4.

4.3. Implementation details

We extracted patches of shape 512×512 with 256×256 degree of overlapping out from each WSI. To avoid redundant information, we focused on patches coming mostly from tissue area. Afterward, we applied a pretrained ResNet50 on each patch to derive their representations. Depending on each experimental setup described further

below, these patches are either at 0.25 or $0.50 \mu\text{m}$ per pixel (mpp), corresponding to $40\times$ or $20\times$ magnification respectively.

For the Transformer baseline models, we constructed both MHSA and MHA with 8 attention heads. For the aggregation layer in particular, according to Eq. (3), it has R of shape 16×2048 . In other words, in each attention head, there are 16 learnable prototypical patterns each of which is described by a 2048-dimensional feature vector. We trained

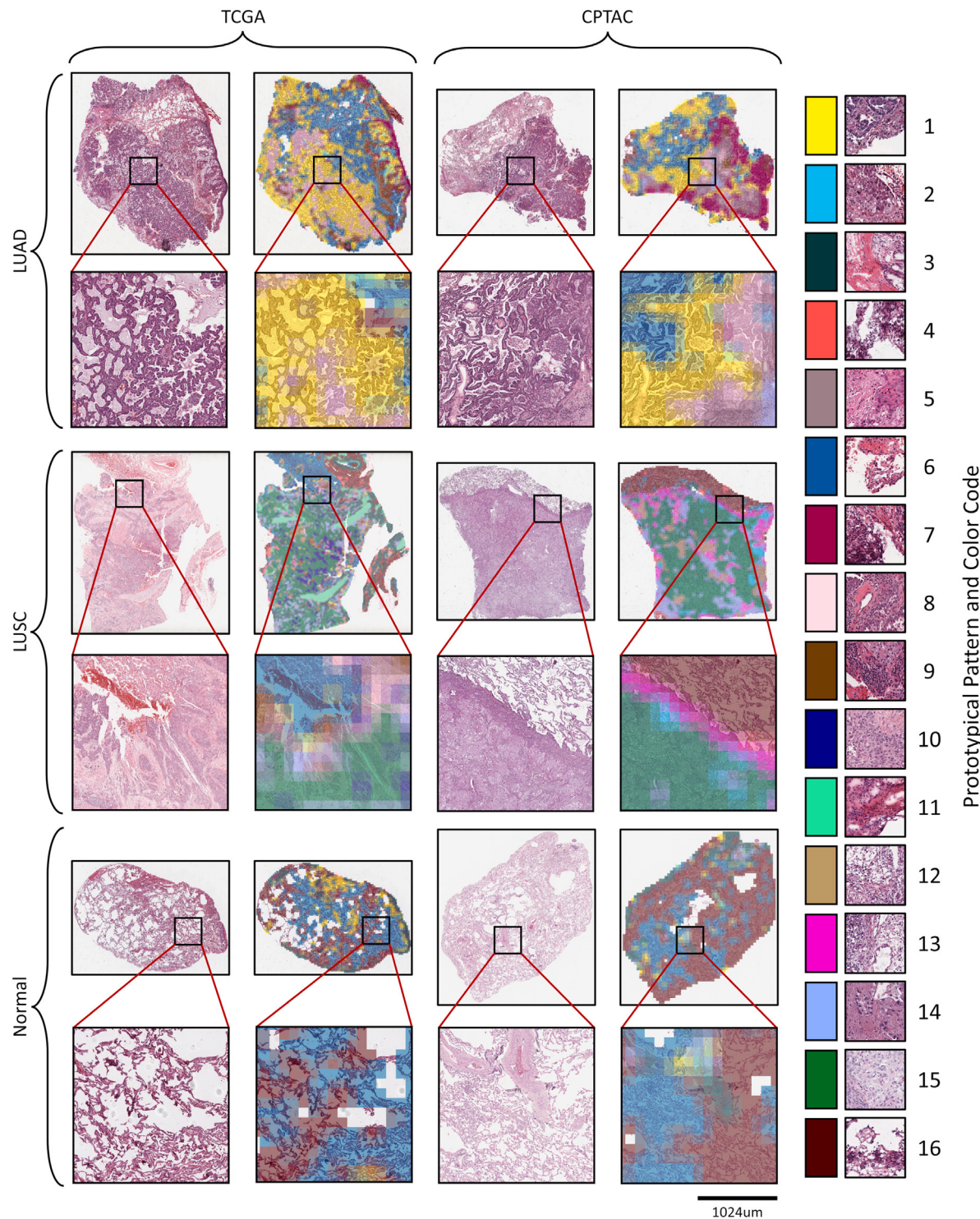


Fig. 4. Visual comparison of the pattern assignment maps (PAMs) of lung tissue between the reference cohort (all WSIs in TCGA) and other cohorts (all WSIs in CPTAC). PAMs were constructed using 16 prototypical patterns. In turn, using SWAV-ResNet50 patch-level features, these patterns were derived based on all WSIs within the TCGA cohort. Overlapping regions have their colors averaged for illustration. Locations whose colors do not align with established color code indicate the transition between assigned patterns. Note that patterns having the same color but were derived from different clustering may not be semantically similar. The colors in Fig. 3 denote the same assignments as this figure. The color assignment is for assessing the consistency within this figure only.

each Transformer model for 50 epochs using Adam optimizer with a learning rate of 0.001. We provide more details about their formulation in the Supplementary Material (Appendix A1).

For experiments related to learning the co-localization of prototypical patterns, we utilized a reduced version of ResNet50 with 34 layers.

To differentiate this from the usual ResNet34, this version uses full bottleneck (3 consecutive convolutional layers with kernel size of 1, 3 and 1) instead of 2 convolutional layers where each has kernel size of 3. Similarly, we also trained this model for 50 epochs using Adam optimizer with a learning rate of 0.001.

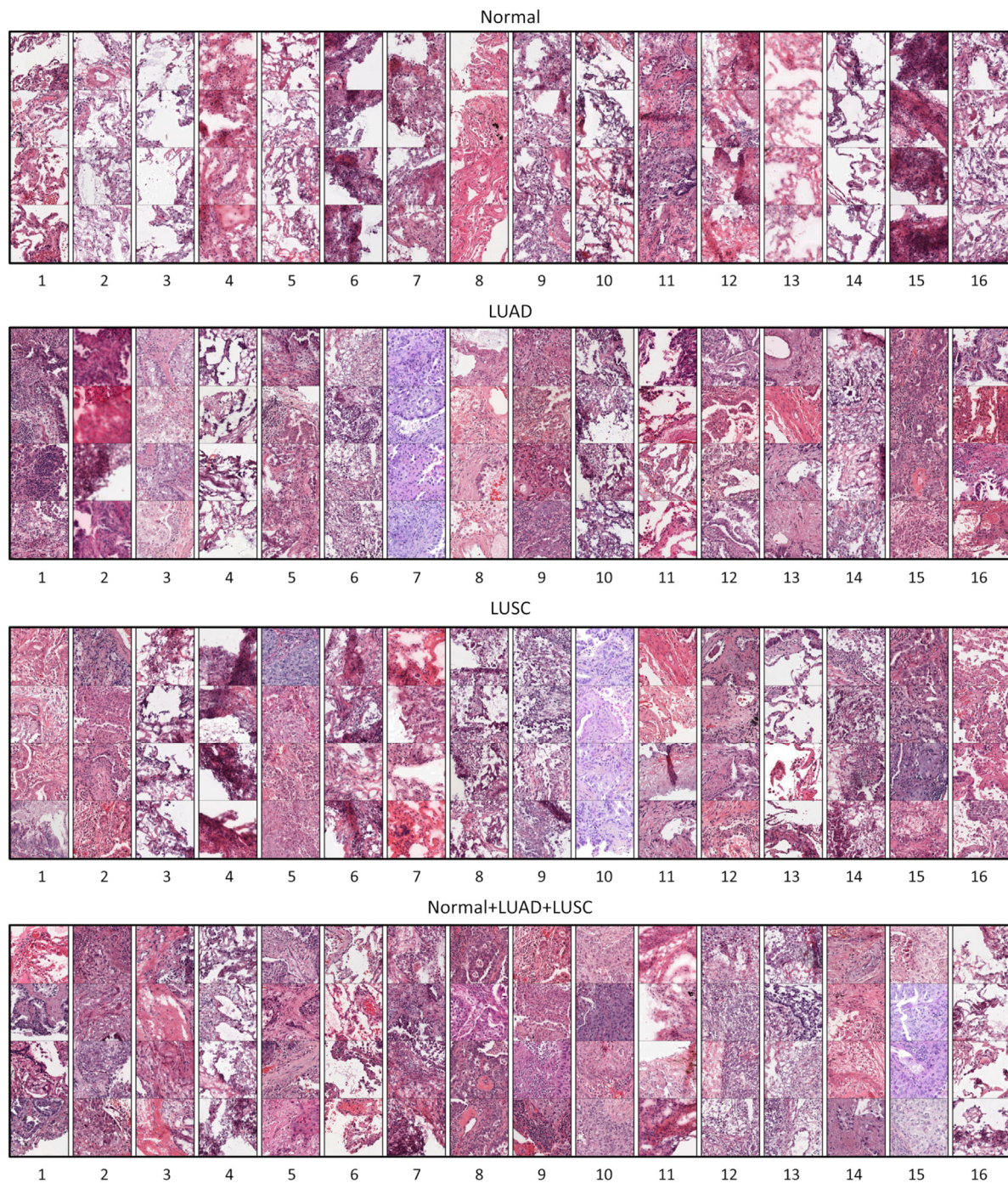


Fig. 5. Visualization of prototypical patterns extracted using solely lung tissue. Four closest patches to each prototypical pattern. There are 16 prototypical patterns derived using SWAV-ResNet50 patch-level features from only Normal WSIs, only LUAD WSIs, only LUSC WSIs or all available WSIs (Normal+LUAD+LUSC) within the TCGA cohort. Within each set of reference tissue (WSIs), the patterns are arranged in a 1×16 (height \times width) grid where each cell contains 4 closest patches.

Regarding linear probing, we trained all the linear layers, which are also known as fully connected layers, for 50 epochs using Adam optimizer with a learning rate of 0.001.

Finally, although we compare our proposal against methods that utilized patch-level features obtained from ResNet34 or ResNet18 pre-trained on histological images, we utilized only patch-level features based on ImageNet to assess our proposal. There are two primary reasons for this decision: (a) models based on ImageNet are widely used and therefore have been extensively assessed, (b) recent research has also shown that models pretrained on histological images may not always provide better performance compared to those trained on

ImageNet, especially for deeper neural networks like ResNet50 (Ciga et al., 2020).

4.4. Prototypical patterns

Before diving deeper into further assessments, it is important to conduct a sanity check on the sets of prototypical patterns we derived from a histological perspective. We constructed 4 sets of prototypical patterns using solely Normal, LUAD, LUSC and all WSIs (Normal+LUAD+LUSC) in the TCGA cohort as reference. Using patch-level representations obtained from SWAV-ResNet50 (Caron et al., 2020), we

extracted 16 prototypical patterns for each set. While the number of prototypical patterns can be different, results from our ablation studies (as reported in Appendix A3.1) have shown that 16 are generally enough to obtain discriminative WSI-level representation.

To validate whether the prototypical patterns and their resulting assignments carry histologically meaningful information, we compare the resulting PAMs against annotations of tumor regions provided by pathologists in Fig. 3. Here, the sample WSIs are taken from the ACDC dataset (Li et al., 2020) while the PAMs were based on patterns obtained when using the entire TCGA lung cohort as the reference cohort. We visually identify that prototypical pattern with ocean blue color (color with code 6) or deep red (16) are closely related to Normal tissue areas. Meanwhile, prototypical patterns with yellow (1) or pink (13) colors are related to tumorous area in LUAD whereas green color (15) is related to LUSC. When considering areas assigned with these tumorous patterns and quantitatively measuring them against the pathologist annotations, we obtained 0.6879 ($p \ll 0.0001$) and 0.8407 ($p \ll 0.0001$) in Pearson correlation coefficient for LUAD and LUSC, respectively. As a side note, we restrict this quantitative measurement only to the two sample WSIs provided above. We also note that the existing annotations from the pathologists are rough. As evident from the illustration in Fig. 3, often they circled an entire area that contains not just tumorous components. Therefore, we only selected one WSI per category that has the best localized annotation. For our purposes, the annotation needs to be more fine-grained and localized. Future work will involve further validation against better sources of ground truth that satisfy such criteria.

Using the same set of prototypical patterns utilized in Fig. 4, we further examine the PAMs between the reference cohort (TCGA) and the unseen cohort (CPTAC) on 3 tissue types: LUAD, LUSC and Normal. From the illustration, although the assignments in unseen cohorts are less distinct compared to the reference set, we observe that the assignments still maintain their consistency from a bird's eye point of view for major tissue components, such as tumorous or stromal regions across WSIs in each cohort. Aligning with our previous observations in Fig. 3, we also observe similar assignments in Fig. 4 for the sample LUAD and LUSC WSIs. Specifically, in both TCGA and CPTAC cohort, we notice that Tumor WSIs contain a large swath of yellow (0) or brown color (14) compared to their normal counterparts. We provide additional examples when using only Normal WSIs as reference set in the Supplementary Materials (Fig. A4).

Since different source of reference tissue results in different set of prototypical patterns, we additionally evaluate how the histological meaning of these sets vary by examining the closest patches assigned to each pattern in Fig. 5 when using Normal, LUAD, LUSC or all WSIs (Normal+LUAD+LUSC) in the TCGA cohort as the reference cohort. From the figure, we observe that patches assigned to the same prototypical pattern are semantically similar.

In conclusion, through a brief visual assessment and a rough quantitative measurement, we postulate that our derived prototypical patterns are histologically meaningful. However, further research is necessary to accurately validate the biological meaning of these sets of prototypical patterns.

4.5. Comparative evaluation

Settings. It is expected that our proposed set of representations should perform at least comparable to methods that are capable of utilizing all patch-level features from the constituent parts (instances) within the WSI, especially in comparison to the baseline Transformers. In order to evaluate this, we restrict our comparison to other multiple instance learning methods that do not involve majority voting of instance predictions within the WSI: MS-MIL-RNN (Campanella et al., 2019), CLAM (Lu et al., 2021), MS-ABMIL (Hashimoto et al., 2020), DSMIL-LC (Li et al., 2021), FocAttn-MIL (Kalra et al., 2021),

HIPT (Chen et al., 2022a) and our two baselines Transformers as described above.

We compared these methods with our proposed representations that were derived by weighted pooling features of patches assigned to each pattern ($\bar{H}\text{-}w$), average pooling features of the top 128 closest patches assigned to each pattern ($\bar{H}\text{-}k128$), learned co-localization of one-hot-encoded PAM (\bar{C} -one-hot) or their combination. In addition to that, we also extracted traditional features: proportion of assigned prototypical patterns \hat{H} within PAM, the co-occurrence matrix \hat{C} from 8 or their combination as additional baselines. For this experiment, we constructed these representations from 16 prototypical patterns when using patch-level representations from SWAV-ResNet50.

Results. We respectively present our results for Normal vs Tumor classification and for LUAD vs LUSC using solely lung tissue in Table 2 and in Table 3. Here, the “Features” column in both tables denotes the encoders for the patch-level representation: SUPERVISE-ResNet50, SWAV-ResNet50 or fine-tuned/retrained a CNN (Tuned). For the last category, this was often performed on pathological dataset rather than ImageNet (Li et al., 2021; Kalra et al., 2021). For WSI-level H2T representation, for simplicity, we only constructed them using patch-level feature from SWAV-ResNet50. In this experiment, CPTAC-LUAD and CPTAC-LUSC were combined to make the CPTAC dataset whereas TCGA-LUAD and TCGA-LUSC were combined to make the TCGA dataset.

In general, we observe that the Transformer models perform better than all recently published methods on both classification tasks. Furthermore, a full Transformer model (transformer-2) is more powerful than its simplified counterpart (transformer-1). Other than that, using better patch-level representation often results in better performance. This is evident with the model achieving the best performance, transformer-2. When moving from SUPERVISE-ResNet50 to SWAV-ResNet50, on average, its AUROC values for Normal vs Tumor were respectively improved by 1.2% (0.963 vs 0.975) for TCGA-test and by 0.63% (0.970 vs 0.976) for CPTAC-test. In case of LUAD vs LUSC, the improvement is 4.7% (0.796 vs 0.843) for TCGA-test and 1.2% (0.911 vs 0.922) for CPTAC-test.

Interestingly, CLAM achieved comparable or slightly better results in comparison to the transformer-2 in some cases. When using SUPERVISE-ResNet50 for Normal vs Tumor, CLAM achieved higher AUROC on average compared to transformer-2 (0.979 vs 0.970) for CPTAC-test. In comparison to transformer-1, CLAM outperformed the model by 0.2% (0.955 vs 0.953) in AUROC on average for TCGA-test. However, when using SWAV-ResNet50, CLAM performance was slightly worse than the transformer-1 on average by 0.3% (0.972 vs 0.970) in AUROC for TCGA-test. Similar phenomena can also be observed for LUAD vs LUSC. As shown in Table 3, when using SWAV-ResNet50, transformer-1 outperformed CLAM by 1.0% (0.928 vs 0.918) in AUROC for CPTAC-test. This discrepancy in CLAM performance when switching the origin of patch-level features can be attributed to the fact that CLAM was designed to tune the patch-level representations. As such, when the features are already highly discriminative in case of SWAV, their proposed loss would reduce the representation power instead.

Regarding our proposed representations, for Normal vs Tumor, when cross-validating within TCGA cohort, $\bar{H}\text{-}w$, $\bar{H}\text{-}k128$ and $\bar{H}\text{-}w+\bar{C}$ -one-hot based on SWAV-ResNet50 achieved more than 0.99 in AUROC and surpassed DSMIL-LC (0.982). Amongst them, $\bar{H}\text{-}k128$ is the most discriminative representation. When being independently tested, $\bar{H}\text{-}k128$ in particular achieved better performance compared to the best model on TCGA-test (transformer-2 based on SWAV-ResNet50) by 0.9% (0.984 vs 0.975); and comparable results compared to the best model on CPTAC-test (CLAM based on SUPERVISE-ResNet50).

On LUAD vs LUSC, $\bar{H}\text{-}k128$ achieved comparable performance in comparison to the best model (transformer-2) when cross-validating. However, it is noticeably worse than other approaches that involves

Table 2

Comparison study on classifying Normal vs Tumor WSIs using solely lung tissue. The proposed H2T representations (\bar{H} and \bar{C}) were derived based on 16 prototypical patterns. These patterns were obtained by using SWAV-ResNet50 patch-level features extracted from all WSIs within each discovery cohort. \bar{H} -w is obtained by weighted summing patch features assigned to a pattern; \bar{H} -k128 is obtained by averaging features from the top 128 closest patches assigned to a pattern; \bar{C} -one-hot is the representation obtained by training CNN on the one-hot-encoded pattern assignment map (PAM); \hat{H} is the histogram of the patterns within PAM; \hat{C} is the co-localization matrix of patterns within PAM. Reported results are mean \pm standard deviation of AUROC taken across 5 stratified folds.

Features	Method	CPTAC-valid	TCGA-test	TCGA-valid	CPTAC-test
Tuned ^a	MS-MIL-RNN ^b (Campanella et al., 2019)	–	–	0.956 \pm 0.000	–
Tuned ^a	MS-ABMIL ^b (Hashimoto et al., 2020)	–	–	0.979 \pm 0.000	–
Tuned ^a	DSMIL-LC ^b (Li et al., 2021)	–	–	0.982 \pm 0.000	–
SUPERVISE-ResNet50 (He et al., 2016)	CLAM ^c (Lu et al., 2021) transformer-1 transformer-2	0.992 \pm 0.003 0.987 \pm 0.009 0.993 \pm 0.005	0.955 \pm 0.007 0.953 \pm 0.009 0.963 \pm 0.004	0.997 \pm 0.002 0.992 \pm 0.002 0.996 \pm 0.001	0.979 \pm 0.002 0.958 \pm 0.005 0.970 \pm 0.003
SWAV-ResNet50 (Caron et al., 2020)	CLAM ^c (Lu et al., 2021) transformer-1 transformer-2	0.994 \pm 0.005 0.993 \pm 0.003 0.992 \pm 0.004	0.970 \pm 0.003 0.972 \pm 0.009 0.975 \pm 0.002	0.995 \pm 0.002 0.996 \pm 0.002 0.996 \pm 0.003	0.971 \pm 0.004 0.961 \pm 0.006 0.976 \pm 0.004
SWAV-ResNet50 (Caron et al., 2020)	\hat{H} \hat{C} $\hat{H} + \hat{C}$ \bar{H} -w \bar{H} -k128 \bar{C} -one-hot \bar{H} -w+ \bar{C} -onehot	0.950 \pm 0.004 0.972 \pm 0.002 0.979 \pm 0.005 0.996 \pm 0.003 0.998 \pm 0.002 0.970 \pm 0.010 0.995 \pm 0.004	0.880 \pm 0.003 0.939 \pm 0.003 0.935 \pm 0.002 0.975 \pm 0.003 0.984 \pm 0.003 0.937 \pm 0.007 0.972 \pm 0.007	0.946 \pm 0.006 0.965 \pm 0.004 0.967 \pm 0.007 0.997 \pm 0.001 0.996 \pm 0.004 0.966 \pm 0.007 0.997 \pm 0.002	0.817 \pm 0.010 0.906 \pm 0.008 0.872 \pm 0.009 0.954 \pm 0.005 0.978 \pm 0.006 0.923 \pm 0.017 0.957 \pm 0.007

^aPretrained CNN was further tuned before being used as a feature extractor by the authors in the original work.

^bResults are taken from Table 2 in Li et al. (2021). The original work did not report the standard deviation, thus we set it to 0.

^cResults are produced by us.

more complicated neural networks. Most notably on TCGA-test, \bar{H} -k128 based on SWAV-ResNet50 achieved only 0.8021 in AUROC in comparison to the worst model under the same setup (0.835 in AUROC of transformer-1 with SWAV-ResNet50).

Meanwhile, although traditional features like \hat{H} , \hat{C} and $\hat{H} + \hat{C}$ could achieve results above 0.90 AUROC in some cases in cross-validation for Normal vs Tumor, they severely lack discriminative power on unseen cohort and are out-competed by other methods. On the other hand, despite showing better results compared to handcrafted features in some situations, in comparison to \bar{H} -w and \bar{H} -k128, representations obtained from learning co-localization (\bar{C}) performed poorly when being used alone in both tasks.

We further evaluated the performance of our proposed method when sub-typing cancers for other tissue types from the same center. We performed CCRCC vs PRCC vs CHRCC on kidney tissue using RCC dataset and IDC vs ILC on breast tissue using BRCA dataset. We present their results in Table 4. For completeness, we also provide results for LUAD vs LUSC (i.e. using NSCLC dataset). Aside from HIPT, all other methods utilized SWAV-ResNet50 features. Among comparative MIL methods, transformer-2 remains the best performing model. We also observe that our proposed methods remain competitive across different tissue types. In RCC, \bar{H} -w achieved similar performance as transformer-2 for AUROC but it has higher mAP. Compared to HIPT, \bar{H} -w AUROC is 0.2% higher. Similarly, for BRCA, \bar{H} -w outperformed transformer-2 by 0.3% and is significantly better than HIPT by 6.5%.

With these results, we demonstrate that the representations from H2T can achieve results comparable to other state-of-the-art approaches. To further understand the difference in performance of these methods, we also performed statistical analysis, the results and details are provided in the Supplementary (Section 5).

4.6. Ablation study

Going along the framework in Fig. 1, we investigate various components that are involved in the derivation of the prototypical patterns and the construction of the subsequent WSI-level H2T representation. Further experiments were conducted and described in Appendix A3.

4.6.1. Representations from co-localization

Settings. The co-localization of clinically-grounded patterns like TILs has shown to be important for clinical settings. Additionally, our results in Tables 2 and 3 suggest that such co-localization features still remain somewhat predictive even when we compute them based on the abstract patterns rather than the clinically-grounded entities (nucleus types). Here, we investigate further on:

- The effect of using one-hot encoding to aid the training process.
- How the representations learned by CNN fare against their hand-crafted counterpart across different sources of prototypical patterns.

The evaluation was conducted by classifying Normal vs Tumor. For this experiment, the prototypical patterns were obtained by using SWAV-ResNet50 features and from all WSIs within the discovery cohort. Accordingly, we compare the discriminative power of: \hat{C} the co-localization matrix of patterns within the pattern assignment map (PAM); \bar{C} -raw the representation obtained by training CNN on the PAM; \bar{C} -one-hot the representation obtained by training CNN on the one-hot-encoded PAM.

Results. From the results in Table 5, we identify that one-hot encoding is critical for training CNNs when using PAMs as input. Regardless of the number of prototypical patterns, without one-hot encoding, the performance would drop up to 0.14 in mAP. Interestingly, for this particular task, representations learned by CNNs performed noticeably better than handcrafted features. However, when using 16 prototypical patterns, the latter performed comparable to the former. This suggests the results may vary for a more difficult task. We provide additional study related to this within the Supplementary Material (Table A6) which further highlights this possibility.

4.6.2. Pooling strategies

Settings. Despite their weaknesses on higher resolution (Table A1), results thus far indicate that our handcrafted formulation in Eq. (7) and the H2T framework can be remarkably competitive compared to the Transformer. We further investigate several different ways to derive the set of weights for Eq. (7). For this experiment, we constructed the WSI-level representation using 16 prototypical patterns and from

Table 3

Comparison study on classifying LUAD vs LUSC WSIs. The proposed H2T representations (\bar{H} and \bar{C}) were derived based on 16 prototypical patterns. These patterns were obtained by using SWAV-ResNet50 patch-level features extracted from all WSIs within each discovery cohort. \bar{H} -w is obtained by weighted summing patch features assigned to a pattern; \bar{H} -k128 is obtained by averaging features from the top 128 closest patches assigned to a pattern; \bar{C} -one-hot is the representation obtained by training CNN on the one-hot-encoded pattern assignment map (PAM); \hat{H} is the histogram of the patterns within PAM; \hat{C} is the co-localization matrix of patterns within PAM. Reported results are mean \pm standard deviation of AUROC taken across 5 stratified folds.

Features	Method	CPTAC-valid	TCGA-test	TCGA-valid	CPTAC-test
Tuned ^a	FocAttn-MIL (Kalra et al., 2021)	–	–	0.920 \pm 0.000	–
SUPERVISE-ResNet50 (He et al., 2016)	CLAM ^b (Lu et al., 2021)	0.967 \pm 0.004	0.791 \pm 0.008	0.927 \pm 0.009	0.907 \pm 0.007
	transformer-1	0.960 \pm 0.009	0.780 \pm 0.005	0.912 \pm 0.006	0.901 \pm 0.009
	transformer-2	0.978 \pm 0.005	0.796 \pm 0.005	0.927 \pm 0.008	0.911 \pm 0.008
SWAV-ResNet50 (Caron et al., 2020)	CLAM ^b (Lu et al., 2021)	0.977 \pm 0.005	0.840 \pm 0.003	0.938 \pm 0.007	0.918 \pm 0.003
	transformer-1	0.979 \pm 0.007	0.835 \pm 0.008	0.937 \pm 0.011	0.928 \pm 0.006
	transformer-2	0.983 \pm 0.008	0.843 \pm 0.005	0.943 \pm 0.012	0.922 \pm 0.003
SWAV-ResNet50 (Caron et al., 2020)	\hat{H}	0.745 \pm 0.025	0.579 \pm 0.001	0.661 \pm 0.016	0.770 \pm 0.005
	\hat{C}	0.859 \pm 0.016	0.638 \pm 0.003	0.732 \pm 0.020	0.791 \pm 0.004
	$\hat{H} + \hat{C}$	0.861 \pm 0.013	0.638 \pm 0.003	0.728 \pm 0.022	0.794 \pm 0.005
	\bar{H} -w	0.972 \pm 0.009	0.788 \pm 0.013	0.927 \pm 0.016	0.903 \pm 0.007
	\bar{H} -k128	0.984 \pm 0.004	0.802 \pm 0.005	0.943 \pm 0.010	0.924 \pm 0.005
	\bar{C} -onehot	0.863 \pm 0.030	0.628 \pm 0.013	0.704 \pm 0.031	0.765 \pm 0.011
	\bar{H} -w+ \bar{C} -onehot	0.983 \pm 0.006	0.789 \pm 0.009	0.919 \pm 0.009	0.904 \pm 0.006

^aPretrained CNN was further tuned before being used as a feature extractor by the authors in the original work. The original work did not report the standard deviation, thus we set it to 0.

^bResults are produced by us.

Table 4

WSI-level cancer sub-typing for kidney (RCC), breast (BRCA), and lung (NSCLC). Reported results are mean \pm standard deviation of AUROC and mAP taken across 5 stratified folds. For RCC sub-typing, we report the macro-averaged AUROC across the three subtypes. The results of NSCLC are partially copied from column TCGA-valid in Table 3. Here, CLAM, transformer-1, transformer-2 and our proposed methods utilized SWAV-ResNet50 features.

Method	RCC		BRCA		NSCLC	
	AUROC	mAP	AUROC	mAP	AUROC	mAP
HIPT ^a (Chen et al., 2022a)	0.980 \pm 0.013	–	0.874 \pm 0.060	–	0.952 \pm 0.021	–
CLAM ^b (Lu et al., 2021)	0.990 \pm 0.001	0.972 \pm 0.003	0.926 \pm 0.012	0.891 \pm 0.017	0.938 \pm 0.007	0.936 \pm 0.007
transformer-1	0.990 \pm 0.001	0.972 \pm 0.007	0.928 \pm 0.012	0.891 \pm 0.018	0.937 \pm 0.011	0.936 \pm 0.012
transformer-2	0.993 \pm 0.002	0.981 \pm 0.005	0.936 \pm 0.011	0.905 \pm 0.016	0.943 \pm 0.012	0.944 \pm 0.012
\hat{C}	0.926 \pm 0.012	0.771 \pm 0.027	0.749 \pm 0.023	0.668 \pm 0.021	0.732 \pm 0.020	0.723 \pm 0.022
\hat{H}	0.864 \pm 0.008	0.677 \pm 0.023	0.722 \pm 0.023	0.635 \pm 0.020	0.660 \pm 0.015	0.647 \pm 0.012
$\hat{H} + \hat{C}$	0.927 \pm 0.009	0.783 \pm 0.029	0.768 \pm 0.014	0.680 \pm 0.017	0.728 \pm 0.022	0.717 \pm 0.024
\bar{H} -k128	0.993 \pm 0.002	0.983 \pm 0.005	0.924 \pm 0.008	0.879 \pm 0.018	0.943 \pm 0.010	0.941 \pm 0.011
\bar{H} -w	0.993 \pm 0.002	0.983 \pm 0.003	0.939 \pm 0.005	0.899 \pm 0.014	0.927 \pm 0.016	0.926 \pm 0.017

^aResults are taken from the original paper.

^bResults are produced by us.

Table 5

Ablation study on WSI-level H2T representations based on the co-localization of prototypical patterns by classifying Normal vs Tumor using solely lung tissue. Using patch-level features from SWAV-ResNet50, all WSIs (Normal+LUAD+LUSC) within the discovery cohort were utilized to derive each set of prototypical patterns. \bar{C} -raw is the representation obtained by training CNN on the pattern assignment map (PAM); \bar{C} -one-hot is the representation obtained by training CNN on the one-hot-encoded PAM; \hat{C} is the co-localization matrix of patterns within PAM. Reported results are mean \pm standard deviation of mAP taken across 5 stratified folds.

# of clusters	Method	CPTAC-valid	TCGA-test	TCGA-valid	CPTAC-test
8	\hat{C}	0.968 \pm 0.002	0.809 \pm 0.002	0.912 \pm 0.008	0.882 \pm 0.007
8	\bar{C} -raw	0.933 \pm 0.019	0.764 \pm 0.010	0.805 \pm 0.036	0.909 \pm 0.006
8	\bar{C} -one-hot	0.902 \pm 0.008	0.952 \pm 0.027	0.867 \pm 0.018	0.916 \pm 0.012
16	\hat{C}	0.971 \pm 0.002	0.851 \pm 0.004	0.915 \pm 0.019	0.897 \pm 0.008
16	\bar{C} -raw	0.934 \pm 0.017	0.744 \pm 0.021	0.799 \pm 0.029	0.826 \pm 0.006
16	\bar{C} -one-hot	0.971 \pm 0.010	0.865 \pm 0.009	0.928 \pm 0.013	0.926 \pm 0.016
32	\hat{C}	0.977 \pm 0.003	0.826 \pm 0.007	0.924 \pm 0.025	0.884 \pm 0.005
32	\bar{C} -raw	0.826 \pm 0.087	0.667 \pm 0.024	0.732 \pm 0.043	0.862 \pm 0.014
32	\bar{C} -one-hot	0.966 \pm 0.012	0.836 \pm 0.017	0.943 \pm 0.009	0.906 \pm 0.010

patch-level features extracted from using either SWAV-ResNet50 or SUPERVISE-ResNet50.

Results. Our results are provided in Table 6. We observe that the source of prototypical patterns remains the utmost important aspect for H2T and can result in a significant difference in performance. In particular, excluding \bar{H} -fk, representations based on SUPERVISE-ResNet50 consistently performs worse than those based on SWAV-ResNet50.

Other than that, given a set of patches assigned to a prototypical pattern, based on the results of \bar{H} -t[X] (where '[X]' is the threshold value), we identify that selecting patches with distances to their assigned prototypical pattern larger than or equal to '[X]' offer no noticeable improvement in performance. In particular, when the threshold is 0.2 ('[X]' = 0.2 or \bar{H} -t0.2), the performance is equal to that of \bar{H} , which has no filtering, across all categories. This suggests that no patches having

Table 6

Ablation study on using different pooling strategies for Eq. (7) constructing WSI-level H2T representations. The task is classifying Normal vs LUAD vs LUSC using solely lung tissue. All available (Normal+LUAD+LUSC) WSIs within the discovery cohort were utilized to derive 16 prototypical patterns. Reported results are mean \pm standard deviation of mAP taken across 5 stratified folds.

Method	SWAV-ResNet50				SUPERVISE-ResNet50			
	CPTAC-valid	TCGA-test	TCGA-valid	CPTAC-test	CPTAC-valid	TCGA-test	TCGA-valid	CPTAC-test
\bar{H}	0.974 \pm 0.005	0.806 \pm 0.008	0.939 \pm 0.015	0.845 \pm 0.006	0.961 \pm 0.006	0.756 \pm 0.004	0.900 \pm 0.011	0.809 \pm 0.008
\bar{H} -w	0.977 \pm 0.002	0.809 \pm 0.008	0.942 \pm 0.015	0.858 \pm 0.006	0.964 \pm 0.007	0.762 \pm 0.007	0.906 \pm 0.008	0.817 \pm 0.009
\bar{H} -t0.2	0.974 \pm 0.005	0.806 \pm 0.008	0.939 \pm 0.015	0.845 \pm 0.006	0.961 \pm 0.006	0.756 \pm 0.004	0.900 \pm 0.011	0.809 \pm 0.008
\bar{H} -t0.3	0.974 \pm 0.006	0.805 \pm 0.008	0.938 \pm 0.016	0.844 \pm 0.006	0.962 \pm 0.005	0.759 \pm 0.004	0.902 \pm 0.010	0.806 \pm 0.006
\bar{H} -t0.4	0.968 \pm 0.007	0.793 \pm 0.013	0.918 \pm 0.011	0.820 \pm 0.011	0.933 \pm 0.010	0.727 \pm 0.007	0.857 \pm 0.010	0.747 \pm 0.004
\bar{H} -t0.5	0.864 \pm 0.014	0.685 \pm 0.011	0.752 \pm 0.023	0.680 \pm 0.008	0.807 \pm 0.008	0.543 \pm 0.014	0.692 \pm 0.020	0.575 \pm 0.006
\bar{H} -t0.6	0.591 \pm 0.030	0.429 \pm 0.004	0.476 \pm 0.022	0.501 \pm 0.006	0.570 \pm 0.008	0.413 \pm 0.005	0.452 \pm 0.024	0.463 \pm 0.005
\bar{H} -t0.7	0.395 \pm 0.006	0.369 \pm 0.002	0.368 \pm 0.008	0.375 \pm 0.001	0.433 \pm 0.022	0.366 \pm 0.003	0.353 \pm 0.005	0.390 \pm 0.004
\bar{H} -k8	0.978 \pm 0.006	0.813 \pm 0.010	0.954 \pm 0.012	0.871 \pm 0.007	0.960 \pm 0.009	0.743 \pm 0.004	0.917 \pm 0.009	0.805 \pm 0.012
\bar{H} -k16	0.979 \pm 0.005	0.820 \pm 0.008	0.953 \pm 0.016	0.883 \pm 0.008	0.968 \pm 0.008	0.752 \pm 0.003	0.917 \pm 0.019	0.821 \pm 0.014
\bar{H} -k32	0.982 \pm 0.005	0.819 \pm 0.006	0.955 \pm 0.016	0.892 \pm 0.008	0.971 \pm 0.008	0.763 \pm 0.004	0.929 \pm 0.021	0.839 \pm 0.015
\bar{H} -k64	0.985 \pm 0.004	0.825 \pm 0.006	0.956 \pm 0.017	0.893 \pm 0.010	0.978 \pm 0.006	0.769 \pm 0.004	0.932 \pm 0.020	0.848 \pm 0.015
\bar{H} -k128	0.984 \pm 0.004	0.825 \pm 0.005	0.957 \pm 0.014	0.890 \pm 0.007	0.979 \pm 0.005	0.775 \pm 0.001	0.933 \pm 0.019	0.855 \pm 0.012
\bar{H} -fk8	0.902 \pm 0.015	0.672 \pm 0.006	0.832 \pm 0.017	0.626 \pm 0.012	0.873 \pm 0.016	0.611 \pm 0.010	0.807 \pm 0.024	0.684 \pm 0.009
\bar{H} -fk16	0.917 \pm 0.015	0.690 \pm 0.008	0.845 \pm 0.018	0.642 \pm 0.013	0.893 \pm 0.007	0.621 \pm 0.009	0.821 \pm 0.023	0.705 \pm 0.012
\bar{H} -fk32	0.929 \pm 0.012	0.713 \pm 0.005	0.863 \pm 0.016	0.661 \pm 0.013	0.902 \pm 0.016	0.641 \pm 0.006	0.852 \pm 0.027	0.725 \pm 0.012
\bar{H} -fk64	0.933 \pm 0.013	0.725 \pm 0.007	0.871 \pm 0.012	0.688 \pm 0.015	0.917 \pm 0.015	0.662 \pm 0.007	0.867 \pm 0.030	0.744 \pm 0.007
\bar{H} -fk128	0.946 \pm 0.010	0.732 \pm 0.010	0.887 \pm 0.012	0.719 \pm 0.015	0.930 \pm 0.014	0.685 \pm 0.010	0.893 \pm 0.010	0.760 \pm 0.007

distances smaller than 0.2. In addition to that, when the thresholds for selection are larger than 0.2, the discriminative power of the resulting WSI-level representation rapidly degrades in comparison to \bar{H} .

The results of \bar{H} -t[X] suggest that patches within a certain distance to their assigned prototypical patterns may be beneficial for the WSI-level representation. This possibility becomes evident from the results of \bar{H} -k[X]. For this set of WSI-level representation, rather than selecting all patches within a certain threshold, we select the '[X]-th' closest patches to its assigned prototypical pattern. We identify that even when using only the 8 closest patches to each pattern, which corresponds to a maximum of 128 patches in total per WSI, it can offer noticeable improvement in comparison to the generic \bar{H} and \bar{H} -w. Furthermore, aligning with previous observations in Tables 2 and 3, selecting the top 32, 64 or 128 patches per pattern provide the most optimal performance. Accordingly, this corresponds to selecting from 512 to 4096 patches at maximum per WSI. As a side note, the maximum here is the theoretical limit because not all patterns have patches assigned to them. This situation has been partially illustrated in Figs. 3 and 4. Therefore, the actual number of selected patches may be less than the theoretical limits.

In contrast to selecting the top closest strategy, selecting the top furthest patch is detrimental to the representation discriminative power in general in comparison to other method. Interestingly, the best \bar{H} -fk[X] (with '[X]' = 128) was able to achieve high cross-validation results. In case like using SUPERVISE-ResNet50, its TCGA-valid result can approach that of \bar{H} .

On a more reserved note, although \bar{H} -w does not offer the same performance as selection-based methods, they maintain a relatively good performance out-of-the-box compared to others while having no tuning parameters.

4.7. Discovery experiments

Now that we have verified that the features from H2T are discriminative enough for downstream analysis, we provide a brief demonstration on how they can be used for other tasks, such as discovering anomalous WSIs.

In this experiment, we first considered TCGA as discovery cohort and CPTAC as independent (evaluation) cohort. Furthermore, we assumed to only know about the Normal WSIs within TCGA. Similar to what we have done so far, we started by deriving the prototypical patterns based on all WSIs that we have access to (the entire TCGA lung

cohort). Afterward, we generated the \bar{H} -w WSIs level representation for all WSIs in both TCGA and CPTAC dataset. Subsequently, we train isolation forest (Liu et al., 2012), a simple machine learning method to score anomaly, on these Normal WSI-level representations for scoring all WSI-level representation in both datasets. Anomalous WSIs (or out of distribution) have their scores lower than those considered to be in distribution.

The results are shown in Fig. 6. Because the WSI-level features we derived are high-dimensional (a matrix of 16×2048 at the very least), for visualization purpose, we utilize UMAP (McInnes et al., 2018) to project these 32768 features down to 2D plane for positioning each WSI. From the TCGA plot, although there are LUAD and LUSC WSIs which have their anomaly scores in orange range (around 0.8), Normal WSIs still have their anomaly scores distinctly higher (dark deep red or above 0.9). Despite that, there is a number of Normal WSIs having anomaly score below 0.7. However, their positions in the figure are noticeably different from the LUAD and LUSC WSIs, this is reflected by a cluster of red dot on the left within the Embedding subplot. As for the CPTAC subplot, the Normal WSIs have their anomaly scores clearly lower compared to those in the TCGA. most of them have less than 0.8 anomaly score and their scores often concentrate around 0.5 ranges. In spite of that, their scores are still noticeably higher than the majority of LUAD and LUSC WSIs which concentrate below 0.3 spectrum. In addition to the anomaly score, the positions of the Normal WSIs are also distinguishable compared to the cluster of Tumor WSIs.

Other than the anomaly score, the unsupervised clustering of the WSIs within Fig. 6 also shows that unsupervised separation of LUAD and LUSC remains difficult. In TCGA, although the positions of LUAD and LUSC WSIs separate into small clusters, these clusters highly intermixed. On CPTAC, LUAD and LUSC seem to occupy the same space.

All in all, these observations indicate that while our proposed representation can be used for discovery process, more research into improving its discriminative power is necessary.

4.8. Runtime complexity

Given the data-hungry nature of deep learning and the increasingly large amount of data that we have to deal with, it is desirable for a method to be computationally cheap as much as possible while still being strongly predictive. We have touched upon the impact of reducing the time for preparing H2T framework (by using less epochs

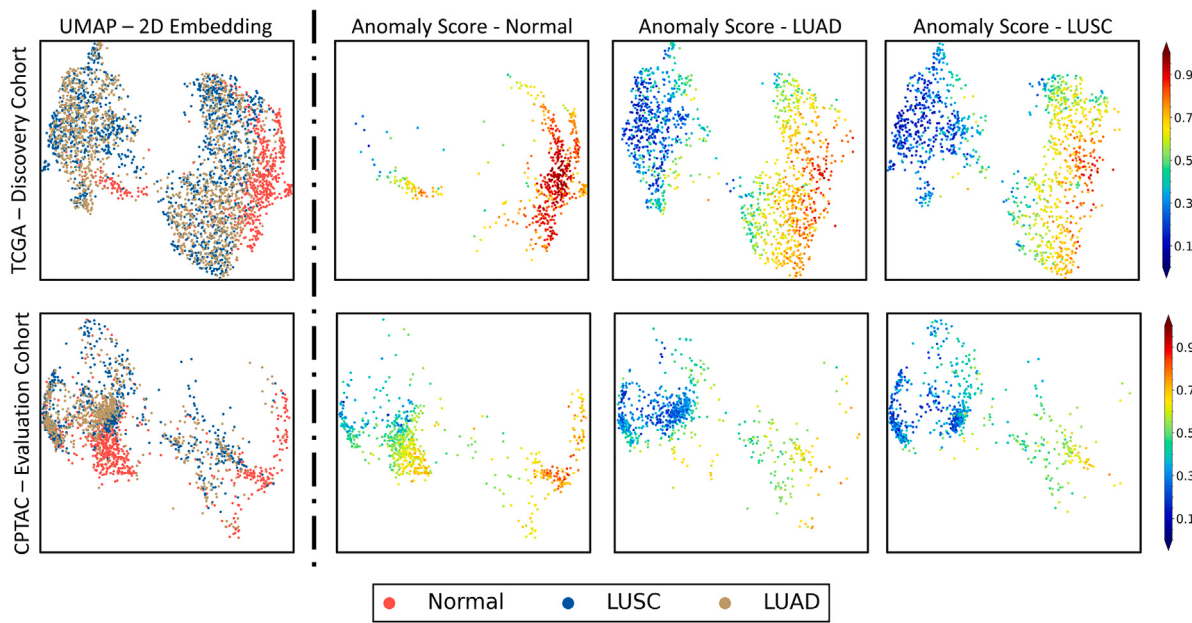


Fig. 6. Discovery study using solely lung tissue. WSI-level H2T representations are projected onto a 2D plane for exploration. The representation was computed based on the prototypical patterns obtained from Normal WSIs (using SWAV-ResNet50 patch-level features) within TCGA (discovery cohort). Here, each data point represents 1 WSI. The projection was done using UMAP, which was also trained by using only WSIs within TCGA. UMAP plots show the sample placements and their labels. Meanwhile, the other plots show the out of distribution (anomaly) score assigned to each sample. The lower the score is, the higher the chance is out of distribution (not Normal).

for clustering) in Fig. A3. Here, we further provide an estimate on the runtime complexity for the Transformer models and our methods in Table 7. We first emphasize that these numbers would vary depending on the systems and should only be taken as reference. The measurements in Table 7 were made using an NVIDIA-A100 GPU when there were no other processes running. All the methods considered here utilized patches at $mpp = 0.50$ and TCGA as discovery cohort. The reported time for training is the average time needed for training 1 single fold split of the TCGA containing an average of 2,560 WSIs. The reported time for feature extraction is the average time taken to finish extracting 1 WSI within the TCGA. On the other hand, the clustering and projection time of H2T are shown for the entire TCGA lung dataset consisting of 3,210 WSIs.

Consistent with the reports in Vaswani et al. (2017), Transformer models are notoriously memory demanding. From Table 7, it is clear that utilizing a full Transformer (transformer-2) or a deeper Transformer (by stacking more multi head self-attention layers) is not possible for common workstation systems. In addition to that, even with a 80 GB A100 GPU and a batch size of 1, it is not possible for us to process many WSIs at $mpp = 0.25$.

In contrast, even when accounting for the clustering times, our H2T is still much cheaper computationally. When processing a single fold (a fold within the stratified split of TCGA discovery cohort), H2T could be 2.6 to 3.6 times faster compared to the Transformer models. Furthermore, due to its small footprint on GPU memory, by running multiple processes in parallel on the same GPU, it is possible to finish the entire training for TCGA as discovery cohort even faster. In particular, with its small footprint, we can fit 4 to 5 running processes within 12 GB of GPU memory, thus bringing the overall differences in processing speed to 10 or 14 times depending on the system. Nonetheless, just like other methods based on patch-level features, feature extraction remains the most time-consuming step.

5. Concluding remarks

Downstream analysis of histopathology images relies on efficient and effective representation of whole slide images (WSIs). In this paper, we proposed a new approach named Handcrafted Histological

Transformer (H2T) for deriving holistic WSI-level representations. We have demonstrated that our derived H2T representations can be readily utilized in both supervised and unsupervised manners with relative ease. In the former setting, we have demonstrated that our set of H2T representations are just as predictive as those obtained from the current best methods, namely the Transformer models. In addition to its effectiveness in representing WSIs, the proposed H2T framework is also more computationally efficient. To the best of our knowledge, H2T is the first handcrafted framework that can compete with the Transformer family while requiring less computational resources.

In general, machine learning systems also have trouble adapting to data coming from different distributions, the so-called *out of distribution* or *OOD* problem. In computational pathology, this can be particularly challenging. Owing to staining and data acquisition practices that vary from center to center, models trained on one center thus may not be directly applicable to data from other centers. It is still an open question as to how we can reliably detect the OOD samples and use them to re-calibrate the system under clinical settings. Nonetheless, despite being more automated and reproducible compared to pathologists, these approaches are still far from being a fully automated system that can discover and stratify diseases. We have also shown how anomaly discovery can be made using the H2T representations in an unsupervised manner. At its core, our method is a handcrafted interpretation on how a black-box Transformer architecture actually performs, thus providing better transparency on the decision-making process of the model. Through the creation and subsequent usage of prototypical patterns, it is also possible to further utilize our established clinical knowledge rather than simply abstract patterns mined from the dataset. We hypothesize that prototypical patterns obtained from clustering a set of representative patches from pathologists can be as effective or may be even more predictive compared to using all available patches. As the WSI-level H2T representation is in a way a projection of a WSI against the established knowledge (i.e., the prototypical patterns that we extracted), it may be used to explore how the patterns evolve along the progression of a disease (Vu et al., 2020).

In this paper, prototypical patterns are extracted from an initial dataset and therefore bounded to a single dataset. A set of prototypical patterns of lung tissue is meaningless for subtyping cancer in breast

Table 7

Runtime complexity of the proposed H2T representation based model and Transformer models. Note that the values here are for reference only as they vary across systems. For our case, the entire experiments were conducted on a single NVIDIA-A100 GPU when there were no other running processes. All the methods under measurement utilized patches at 0.5 μm per pixel and TCGA as discovery cohort. The reported time for training is the average time needed for training 1 single fold split of the TCGA (containing an average of 2,560 WSIs). The reported time for feature extraction is the average time taken to finish extracting 1 WSI within the TCGA. On the other hand, the clustering and projection time of H2T were taken for the entire TCGA dataset.

Metrics	Steps	transformer-1	transformer-2	H2T
Time	Features Extraction	2 min/WSI	2 min/WSI	2 min/WSI
	Clustering	–	–	7 min
	Projection	–	–	3 min
	Training	110 min/fold	80 min/fold	14 min/fold
GPU	Batch Size	8	4	32
	Memory	40 GB	130 GB	2 GB

tissue. Even in the same tissue, a set of prototypical patterns extracted from a subset of lung disease surely would not reflect another. One would assume simply redoing the process using a larger dataset is enough to amend the problem. However, it is not realistic to have *data for all* diseases. In addition, the computation cost of such operation would increase exponentially each time the dataset gets expanded. To alleviate this problem, it is important to investigate how a set of prototypical patterns from one dataset can be considered as “novel” compared to those extracted using another dataset as well as how we can combine these sets of prototypical patterns together.

Parallel to the above, further investigations on how to automatically and systematically obtain better prototypical patterns is also important. In the scope of this work, we investigated the plausibility of our proposal extensively by using k-means due to its simplicity. There are better clustering techniques that are available. Dictionary learning is another promising research direction given how the prototypical patterns are obtained and utilized. Lastly, given the close relationship between Transformer-based method and CBIR system, investigating on the potential use of H2T as an approximation of a subset of Transformers for a CBIR task may open new research directions in the nascent area of computational pathology. Additionally, while the capability of Transformer-based models for CBIR in natural images has been well demonstrated (Chen et al., 2022b), it is relative unknown how well they would fare on other medical image processing tasks and thus further research is also required.

Given the robustness and representation power of massive Transformer models like GPT-3, it is also of interest to pretrain a Transformer model end-to-end for computational pathology. However, the massive scale of WSIs at high magnification level presents a huge technical challenge for such an attempt. In light of this challenge, we consider an intermediate compressed representation of a WSI (such as the H2T representation) or multi-stage pretraining as in Chen et al. (2022a) as two possible novel directions for end-to-end training for WSI-level analysis.

Through the H2T framework, we have also shown how WSI-level representation can be disentangled into instance-level patterns and co-localization of instance-level patterns. This disentanglement thus allows us to explore how each representation contributes toward the overall predictive power of the final WSI-level representation. Given the reduction in predictive power of co-localization representation in some tasks, we hypothesize that a prototypical pattern that is a combination of both patch co-localization and patch-level features can be a strong alternative for a better WSI-level representation.

While we have successfully derived representations at WSI-level and were able to use them to identify anomalous WSIs, identifying which patches in each WSI that contribute in turning the WSI into an anomaly remains difficult. Because these patches potentially indicate new tissue phenotype, without a way to go from WSI-level back to patch-level, explainable prediction and automated identification of disease may not be possible as we still rely on pathologists for reviewing all possible anomalous WSI cases. In addition, so far we have only demonstrated

anomalous detection on a very narrow and easy scope of categories, namely Normal vs Tumor in lung tissue. Our method is not yet able to reliably highlight the cancer subtypes. Further research is required to further enhance its discriminative power.

Meanwhile, although our framework can provide more transparency compared to other methods, our prototypical patterns are still much more abstract compared to known patterns, such as the number of TILs. Within this study, while we have provided a high-level assessment of the possible histological meaning associated with our prototypical patterns, this was conducted only on a small number of WSIs. Therefore, in order to utilize our prototypical patterns and their WSI-level representation for more clinically related tasks, it is necessary to investigate their histological meaning on a larger scale.

We have uncovered and further confirmed existing practice in machine learning, namely keeping an independent testing set is extremely important to correctly assess the results. Specifically, in the scope of our dataset and tasks, despite each cohort containing thousands of WSIs, we have shown that high cross-validation results within each cohort may not be enough to identify good approaches. This is evident through our ablation study on pooling strategies. Here, in spite of having high performance on cross-validation, many of our models fall short on the evaluation set.

Self-supervised learning in natural images has relied on the complexity of ImageNet to measure progress in the field. Much of the complexity associated with ImageNet can be partly attributed to its size (millions of images) and the large number of present categories, that are structured in a meaningful hierarchy. In comparison, although the largest publicly available dataset in computational pathology also contains thousands of WSIs (TCGA), there is less variation between its categories. As a result, we believe curating a new dataset may be necessary to further develop and investigate WSI-level representations in computational pathology. Specifically, this dataset should be a large collection of extensively stratified diseases (such as cancer grades of all tissue types).

Finally, unlike image patch classification, localization of disease sites as well as anomaly or novelty detection are intrinsically intertwined for processing WSIs. Future work will involve performing localization in an unsupervised manner and further validation on more disease variations.

Declaration of competing interest

The authors declare that they have no known competing financial interests or personal relationships that could have appeared to influence the work reported in this paper.

Data availability

We provide the code and the intermediate data (deep features and associated patterns) at <https://github.com/vqdang/H2T> to facilitate future investigation efforts.

Acknowledgments

We thank Rob Jewsbury and Simon Graham for their invaluable feedback during the write-up of the manuscript. Quoc Dang Vu is funded by The Royal Marsden NHS Foundation Trust. NR and SR are part of the PathLAKE digital pathology consortium, which is partly funded from the Data to Early Diagnosis and Precision Medicine strand of the governments Industrial Strategy Challenge Fund, managed and delivered by UK Research and Innovation (UKRI). NR and SR are also funded by the European Research Council (funding call H2020 IM2-RIA). NR was also supported by the UK Medical Research Council (grant award MR/P015476/1), Royal Society Wolfson Merit Award and the Alan Turing Institute.

Appendix A. Supplementary data

Supplementary material related to this article can be found online at <https://doi.org/10.1016/j.media.2023.102743>. The supplementary contains additional ablation experiments which explore the effects of various parameters within our proposed method. Additionally, we also performed experiments on stratifying diseases using solely prototypical patterns that were extracted from normal tissue.

References

- Abbet, C., Zlobec, I., Bozorgtabar, B., Thiran, J.P., 2020. Divide-and-rule: Self-supervised learning for survival analysis in colorectal cancer. In: MICCAI.
- Abels, E., Pantanowitz, L., Aeffner, F., Zarella, M., Laak, J., Bui, M., Vemuri, V., Parwani, A., Gibbs, J., Agosto-Arroyo, E., Beck, A., Kozlowski, C., 2019. Computational pathology definitions, best practices, and recommendations for regulatory guidance: A white paper from the digital pathology association. *J. Pathol.* 249, <http://dx.doi.org/10.1002/path.5331>.
- Amgad, M., Elfandy, H., Hussein, H., Atteya, L.A., Elsebaie, M.A., Abo Elnasr, L.S., Sakr, R.A., Salem, H.S., Ismail, A.F., Saad, A.M., et al., 2019. Structured crowdsourcing enables convolutional segmentation of histology images. *Bioinformatics* 35 (18), 3461–3467.
- Andrews, S., Tschantaridis, I., Hofmann, T., 2002. Support vector machines for multiple-instance learning. In: NIPS, Vol. 2, No. 3. p. 7.
- Awan, R., Sirinukunwattana, K., Epstein, D., Jefferyes, S., Qidwai, U., Aftab, Z., Mujeeb, I., Snead, D., Rajpoot, N., 2017. Glandular morphometrics for objective grading of colorectal adenocarcinoma histology images. *Sci. Rep.* 7 (1), 16852. <http://dx.doi.org/10.1038/s41598-017-16516-w>.
- Azam, A.S., Miligy, I.M., Kimani, P.K.-U., Maqbool, H., Hewitt, K., Rajpoot, N.M., Snead, D.R.J., 2021. Diagnostic concordance and discordance in digital pathology: a systematic review and meta-analysis. *J. Clin. Pathol.* 74 (7), 448–455. <http://dx.doi.org/10.1136/jclinpath-2020-206764>, arXiv:<https://jcp.bmjjournals.org/content/74/7/448.full.pdf>, URL: <https://jcp.bmjjournals.org/content/74/7/448>.
- Bilal, M., Raza, S.E.A., Azam, A., Graham, S., Ilyas, M., Cree, I.A., Snead, D., Minhas, F., Rajpoot, N.M., 2021. Development and validation of a weakly supervised deep learning framework to predict the status of molecular pathways and key mutations in colorectal cancer from routine histology images: a retrospective study. *Lancet Digit. Health* 3 (12), e763–e772.
- Brown, T.B., Mann, B., Ryder, N., Subbiah, M., Kaplan, J., Dhariwal, P., Neelakantan, A., Shyam, P., Sastry, G., Askell, A., Agarwal, S., Herbert-Voss, A., Krueger, G., Henighan, T., Child, R., Ramesh, A., Ziegler, D.M., Wu, J., Winter, C., Hesse, C., Chen, M., Sigler, E., Litwin, M., Gray, S., Chess, B., Clark, J., Berner, C., McCandlish, S., Radford, A., Sutskever, I., Amodei, D., 2020. Language models are few-shot learners, CoRR abs/2005.14165. arXiv:2005.14165.
- Campanella, G., Hanna, M.G., Geneslaw, L., Miraflor, A., Werneck Krauss Silva, V., Busam, K.J., Brogi, E., Reuter, V.E., Klimstra, D.S., Fuchs, T.J., 2019. Clinical-grade computational pathology using weakly supervised deep learning on whole slide images. *Nature Med.*
- Cao, Y., Zhu, L.Z., Jiang, M.J., Yuan, Y., 2016. Clinical impacts of a micropapillary pattern in lung adenocarcinoma: a review. *OncoTargets Ther.* 9, 149.
- Carion, N., Massa, F., Synnaeve, G., Usunier, N., Kirillov, A., Zagoruyko, S., 2020. End-to-end object detection with transformers, CoRR abs/2005.12872. arXiv:2005.12872.
- Caron, M., Misra, I., Mairal, J., Goyal, P., Bojanowski, P., Joulin, A., 2020. Unsupervised learning of visual features by contrasting cluster assignments. In: Proceedings of Advances in Neural Information Processing Systems. NeurIPS.
- Chen, R.J., Chen, C., Li, Y., Chen, T.Y., Trister, A.D., Krishnan, R.G., Mahmood, F., 2022a. Scaling vision transformers to gigapixel images via hierarchical self-supervised learning. In: Proceedings of the IEEE/CVF Conference on Computer Vision and Pattern Recognition. pp. 16144–16155.
- Chen, T., Kornblith, S., Norouzi, M., Hinton, G., 2020. A simple framework for contrastive learning of visual representations. In: International Conference on Machine Learning. PMLR, pp. 1597–1607.
- Chen, W., Liu, Y., Wang, W., Bakker, E.M., Georgiou, T., Fieguth, P., Liu, L., Lew, M.S., 2022b. Deep learning for instance retrieval: A survey. *IEEE Trans. Pattern Anal. Mach. Intell.* 1–20. <http://dx.doi.org/10.1109/TPAMI.2022.3218591>.
- Ciga, O., Xu, T., Martel, A.L., 2020. Self supervised contrastive learning for digital histopathology. arXiv preprint arXiv:2011.13971.
- Diao, J.A., Wang, J.K., Chui, W.F., Mountain, V., Gullapalli, S.C., Srinivasan, R., Mitchell, R.N., Glass, B., Hoffman, S., Rao, S.K., Maheshwari, C., Lahiri, A., Prakash, A., McLoughlin, R., Kerner, J.K., Resnick, M.B., Montalto, M.C., Khosla, A., Wapinski, I.N., Beck, A.H., Elliott, H.L., Taylor-Weiner, A., 2021. Human-interpretable image features derived from densely mapped cancer pathology slides predict diverse molecular phenotypes. *Nature Commun.* 12 (1), 1613. <http://dx.doi.org/10.1038/s41467-021-21896-9>.
- Dietterich, T.G., Lathrop, R.H., Lozano-Pérez, T., 1997. Solving the multiple instance problem with axis-parallel rectangles. *Artificial Intelligence* 89 (1–2), 31–71.
- Djolonga, J., Yung, J., Tschannen, M., Romijnders, R., Beyer, L., Kolesnikov, A., Puigcerver, J., Minderer, M., D'Amour, A., Moldovan, D., et al., 2021. On robustness and transferability of convolutional neural networks. In: Proceedings of the IEEE/CVF Conference on Computer Vision and Pattern Recognition. pp. 16458–16468.
- Doersch, C., Zisserman, A., 2017. Multi-task self-supervised visual learning. In: Proceedings of the IEEE International Conference on Computer Vision. pp. 2051–2060.
- Dosovitskiy, A., Beyer, L., Kolesnikov, A., Weissenborn, D., Zhai, X., Unterthiner, T., Dehghani, M., Minderer, M., Heigold, G., Gelly, S., Uszkoreit, J., Houlsby, N., 2020. An image is worth 16x16 words: Transformers for image recognition at scale, CoRR abs/2010.11929. arXiv:2010.11929.
- Elston, C., Ellis, I., 1991. Pathological prognostic factors in breast cancer. I. The value of histological grade in breast cancer: experience from a large study with long-term follow-up. *Histopathology* 19 (5), 403–410. <http://dx.doi.org/10.1111/j.1365-2559.1991.tb00229.x>, URL: <https://onlinelibrary.wiley.com/doi/abs/10.1111/j.1365-2559.1991.tb00229.x>.
- Gentles, A., Newman, A., Liu, C., Bratman, S., Feng, W., Kim, D., Nair, V., Xu, Y., Khuong, A., Hoang, C., Diehn, M., West, R., Plevritis, S., Alizadeh, A., 2015. The prognostic landscape of genes and infiltrating immune cells across human cancers. *Nature Med.* 21, <http://dx.doi.org/10.1038/nm.3909>.
- Goldstraw, P., Chansky, K., Crowley, J., Rami-Porta, R., Asamura, H., Eberhardt, W.E., Nicholson, A.G., Groome, P., Mitchell, A., Bolejack, V., Goldstraw, P., Rami-Porta, R., Asamura, H., Ball, D., Beer, D.G., Beynon, R., Bolejack, V., Chansky, K., Crowley, J., Dettberbeck, F., Erich Eberhardt, W.E., Edwards, J., Galateau-Sallé, F., Giroux, D., Gleeson, F., Groome, P., Huang, J., Kennedy, C., Kim, J., Kim, Y.T., Kingsbury, L., Kondo, H., Krasnik, M., Kubota, K., Lerut, A., Lyons, G., Marino, M., Marom, E.M., van Meerbeek, J., Mitchell, A., Nakano, T., Nicholson, A.G., Nowak, A., Peake, M., Rice, T., Rosenzweig, K., Ruffini, E., Rusch, V., Sajio, N., Van Schil, P., Sculier, J.P., Shemanski, L., Stratton, K., Suzuki, K., Tachimori, Y., Thomas, C.F., Travis, W., Tsao, M.S., Turrisi, A., Vansteenkiste, J., Watanabe, H., Wu, Y.L., Baas, P., Erasmus, J., Hasegawa, S., Imai, K., Kernstine, K., Kindler, H., Krug, L., Nackaerts, K., Pass, H., Rice, D., Falkson, C., Filosso, P.L., Giaccone, G., Kondo, K., Lucchi, M., Okumura, M., Blackstone, E., Abad Cavaco, F., Ansótegui Barrera, E., Abal Arca, J., Parente Lamelas, I., Arnau Obrer, A., Guijarro Jorge, R., Ball, D., Bascom, G., Blanco Orozco, A., González Castro, M., Blum, M., Chimondegu, D., Cvijanovic, V., Defranchi, S., de Olazí Navarro, B., Escobar Campuzano, I., Macía Vidueira, I., Fernández Araujo, E., Andreo García, F., Fong, K., Francisco Corral, G., Cerezo González, S., Freixinet Gilart, J., García Arangüena, L., García Barajas, S., Girard, P., Goksé, T., González Budíño, M., González Casaurán, G., Gullón Blanco, J., Hernández Hernández, J., Hernández Rodríguez, H., Herrero Collantes, J., Iglesias Heras, M., Izquierdo Elena, J., Jakobsen, E., Kostas, S., León Atance, P., Núñez Ares, A., Liao, M., Losanovsky, M., Lyons, G., Magaroles, R., De Esteban Júlvez, L., Marián Gorospe, M., McCaughan, B., Kennedy, C., Melchor Íñiguez, R., Miravet Sorribes, L., Narango Gozalo, S., Álvarez de Arriba, C., Núñez Delgado, M., Padilla Alarcón, J., Peñalver Cuesta, J., Park, J., Pass, H., Pavón Fernández, M., Rosenberg, M., Ruffini, E., Rusch, V., Sánchez de Cos Escuín, J., Saura Vinuesa, A., Serra Mitjans, M., Strand, T., Subotic, D., Swisher, S., Terra, R., Thomas, C., Tournoy, K., Van Schil, P., Velasquez, M., Wu, Y., Yokoi, K., 2016. The IASLC lung cancer staging project: Proposals for revision of the TNM stage groupings in the forthcoming (eighth) edition of the TNM classification for lung cancer. *J. Thorac. Oncol.* 11 (1), 39–51. <http://dx.doi.org/10.1016/j.jtho.2015.09.009>, URL: <https://www.sciencedirect.com/science/article/pii/S1556086415000179>.
- Graham, S., Epstein, D., Rajpoot, N., 2020. Dense steerable filter cnns for exploiting rotational symmetry in histology images. *IEEE Trans. Med. Imaging* 39 (12), 4124–4136.
- Graham, S., Vu, Q.D., Raza, S.E.A., Azam, A., Tsang, Y.W., Kwak, J.T., Rajpoot, N., 2019. Hover-net: Simultaneous segmentation and classification of nuclei in multi-tissue histology images. *Med. Image Anal.* 101563.
- Gurcan, M.N., Boucheron, L.E., Can, A., Madabhushi, A., Rajpoot, N.M., Yener, B., 2009. Histopathological image analysis: A review. *IEEE Rev. Biomed. Eng.* 2, 147–171. <http://dx.doi.org/10.1109/RBME.2009.2034865>.

- Hamilton, P., Anderson, N., Bartels, P., Thompson, D., 1994. Expert system support using Bayesian belief networks in the diagnosis of fine needle aspiration biopsy specimens of the breast. *J. Clin. Pathol.* 47 (4), 329–336. <http://dx.doi.org/10.1136/jcp.47.4.329>, URL: <https://europemc.org/articles/PMC501936>.
- Hashimoto, N., Fukushima, D., Koga, R., Takagi, Y., Ko, K., Kohno, K., Nakaguro, M., Nakamura, S., Hontani, H., Takeuchi, I., 2020. Multi-scale domain-adversarial multiple-instance CNN for cancer subtype classification with non-annotated histopathological images, CoRR abs/2001.01599. [arXiv:2001.01599](https://arxiv.org/abs/2001.01599).
- He, K., Zhang, X., Ren, S., Sun, J., 2016. Deep residual learning for image recognition. In: Proceedings of the IEEE Conference on Computer Vision and Pattern Recognition. pp. 770–778.
- Hendrycks, D., Mazeika, M., Kadavath, S., Song, D., 2019. Using self-supervised learning can improve model robustness and uncertainty. arXiv preprint [arXiv:1906.12340](https://arxiv.org/abs/1906.12340).
- Hendrycks, D., Zhao, K., Basart, S., Steinhardt, J., Song, D., 2021. Natural adversarial examples. In: Proceedings of the IEEE/CVF Conference on Computer Vision and Pattern Recognition. pp. 15262–15271.
- Hou, L., Samaras, D., Kirc, T.M., Gao, Y., Davis, J.E., Saltz, J.H., 2016. Patch-based convolutional neural network for whole slide tissue image classification. In: 2016 IEEE Conference on Computer Vision and Pattern Recognition. CVPR, IEEE Computer Society, Los Alamitos, CA, USA, pp. 2424–2433. <http://dx.doi.org/10.1109/CVPR.2016.266>, URL: <https://doi.ieeecomputersociety.org/10.1109/CVPR.2016.266>.
- Ilse, M., Tomczak, J.M., Welling, M., 2018. Attention-based deep multiple instance learning, CoRR abs/1802.04712. [arXiv:1802.04712](https://arxiv.org/abs/1802.04712).
- Jumper, J., Evans, R., Pritzel, A., Green, T., Figurnov, M., Ronneberger, O., Tunyasuvunakool, K., Bates, R., Žídek, A., Potapenko, A., et al., 2021. Highly accurate protein structure prediction with AlphaFold. *Nature* 596 (7873), 583–589.
- Kalra, S., Adnan, M., Hemati, S., Dehkharhanian, T., Rahnamayan, S., Tizhoosh, H., 2021. Pay attention with focus: A novel learning scheme for classification of whole slide images. [arXiv:2106.06623](https://arxiv.org/abs/2106.06623).
- Kandemir, M., Hamprecht, F.A., 2015. Computer-aided diagnosis from weak supervision: A benchmarking study. *Comput. Med. Imaging Graph.* 42, 44–50.
- Kather, J.N., Krisam, J., Charoentong, P., Luedde, T., Herpel, E., Weis, C.A., Gaiser, T., Marx, A., Valous, N.A., Ferber, D., et al., 2019. Predicting survival from colorectal cancer histology slides using deep learning: A retrospective multicenter study. *PLoS Med.* 16 (1), e1002730.
- Keenan, S.J., Diamond, J., Glenn McCluggage, W., Bharucha, H., Thompson, D., Bartels, P.H., Hamilton, P.W., 2000. An automated machine vision system for the histological grading of cervical intraepithelial neoplasia (CIN). *J. Pathol.* 192 (3), 351–362.
- Kim, D., Cho, D., Kweon, I.S., 2019. Self-supervised video representation learning with space-time cubic puzzles. In: Proceedings of the AAAI Conference on Artificial Intelligence, Vol. 33, No. 01. pp. 8545–8552.
- Koohbanani, N.A., Unnikrishnan, B., Khurram, S.A., Krishnaswamy, P., Rajpoot, N., 2021. Self-path: Self-supervision for classification of pathology images with limited annotations. *IEEE Trans. Med. Imaging* 40 (10), 2845–2856.
- Kromp, F., Bozsaky, E., Rifatbegovic, F., Fischer, L., Ambros, M., Berneder, M., Weiss, T., Lazic, D., Dörr, W., Hanbury, A., et al., 2020. An annotated fluorescence image dataset for training nuclear segmentation methods. *Sci. Data* 7 (1), 1–8.
- Kwak, J.T., Hewitt, S.M., 2017. Multiview boosting digital pathology analysis of prostate cancer. *Comput. Methods Programs Biomed.* 142, 91–99. <http://dx.doi.org/10.1016/j.cmpb.2017.02.023>, URL: <https://www.sciencedirect.com/science/article/pii/S0169260716306952>.
- Li, B., Li, Y., Elieci, K.W., 2021. Dual-stream multiple instance learning network for whole slide image classification with self-supervised contrastive learning. In: Proceedings of the IEEE/CVF Conference on Computer Vision and Pattern Recognition. CVPR, pp. 14318–14328.
- Li, Z., Zhang, J., Tan, T., Teng, X., Sun, X., Zhao, H., Liu, L., Xiao, Y., Lee, B., Li, Y., et al., 2020. Deep learning methods for lung cancer segmentation in whole-slide histopathology images—the acdc@ lunghp challenge 2019. *IEEE J. Biomed. Health Inf.*
- Liu, F.T., Ting, K.M., Zhou, Z.H., 2012. Isolation-based anomaly detection. *ACM Trans. Knowl. Discov. Data (TKDD)* 6 (1), 1–39.
- Lu, M.Y., Williamson, D.F.K., Chen, T.Y., Chen, R.J., Barbieri, M., Mahmood, F., 2021. Data-efficient and weakly supervised computational pathology on whole-slide images. *Nat. Biomed. Eng.* 5 (6), 555–570. <http://dx.doi.org/10.1038/s41551-020-00682-w>.
- Mari, C.R., Varas Gonzalez, D., Bou-Balust, E., 2022. Multi-scale transformer-based feature combination for image retrieval. In: 2022 IEEE International Conference on Image Processing. ICIP, pp. 3166–3170. <http://dx.doi.org/10.1109/ICIP46576.2022.9897512>.
- McInnes, L., Healy, J., Melville, J., 2018. Umap: Uniform manifold approximation and projection for dimension reduction. arXiv preprint [arXiv:1802.03426](https://arxiv.org/abs/1802.03426).
- Myronenko, A., Xu, Z., Yang, D., Roth, H.R., Xu, D., 2021. Accounting for dependencies in deep learning based multiple instance learning for whole slide imaging. In: International Conference on Medical Image Computing and Computer-Assisted Intervention. Springer, pp. 329–338.
- Ramsauer, H., Schaf, B., Lehner, J., Seidl, P., Widrich, M., Gruber, L., Holzleitner, M., Pavlovic, M., Sandve, G.K., Greiff, V., Kreil, D.P., Kopp, M., Klambauer, G., Brandstetter, J., Hochreiter, S., 2020. Hopfield networks is all you need, CoRR abs/2008.02217. [arXiv:2008.02217](https://arxiv.org/abs/2008.02217).
- Sertel, O., Kong, J., Shimada, H., Catalyurek, U.V., Saltz, J.H., Gurcan, M.N., 2009. Computer-aided prognosis of neuroblastoma on whole-slide images: Classification of stromal development. *Pattern Recognit.* 42 (6), 1093–1103.
- Shaban, M., Khurram, S.A., Fraz, M.M., Alsubaie, N., Masood, I., Mushtaq, S., Hassan, M., Loya, A., Rajpoot, N.M., 2019. A novel digital score for abundance of tumour infiltrating lymphocytes predicts disease free survival in oral squamous cell carcinoma. *Sci. Rep.* 9 (1), 1–13.
- Shield, K.D., Ferlay, J., Jemal, A., Sankaranarayanan, R., Chaturvedi, A.K., Bray, F., Soerjomataram, I., 2017. The global incidence of lip, oral cavity, and pharyngeal cancers by subsite in 2012. *CA: Cancer J. Clin.* 67 (1), 51–64.
- Solis, L.M., Behrens, C., Raso, M.G., Lin, H.Y., Kadara, H., Yuan, P., Galindo, H., Tang, X., Lee, J.J., Kalhor, N., et al., 2012. Histologic patterns and molecular characteristics of lung adenocarcinoma associated with clinical outcome. *Cancer* 118 (11), 2889–2899.
- Tabesh, A., Teverovskiy, M., Pang, H.Y., Kumar, V.P., Verbel, D., Kotsianti, A., Saidi, O., 2007. Multifeature prostate cancer diagnosis and gleason grading of histological images. *IEEE Trans. Med. Imaging* 26 (10), 1366–1378. <http://dx.doi.org/10.1109/TMI.2007.898536>.
- Tan, F., Yuan, J., Ordóñez, V., 2021. Instance-level image retrieval using reranking transformers. In: Proceedings of the IEEE/CVF International Conference on Computer Vision. pp. 12105–12115.
- Van der Maaten, L., Hinton, G., 2008. Visualizing data using t-sne. *J. Mach. Learn. Res.* 9 (11).
- Vaswani, A., Shazeer, N., Parmar, N., Uszkoreit, J., Jones, L., Gomez, A.N., Kaiser, L., Polosukhin, I., 2017. Attention is all you need, CoRR abs/1706.03762. [arXiv:1706.03762](https://arxiv.org/abs/1706.03762).
- Verma, R., Kumar, N., Patil, A., Kurian, N.C., Rane, S., Graham, S., Vu, Q.D., Zwager, M., Raza, S.E.A., Rajpoot, N., Wu, X., Chen, H., Huang, Y., Wang, L., Jung, H., Brown, G.T., Liu, Y., Liu, S., Jahromi, S.A.F., Khani, A.A., Montahaei, E., Baghshah, M.S., Behroozai, H., Semkin, P., Rassadan, A., Dutandie, P., Lodaya, R., Baid, U., Baheti, B., Talbar, S., Mahbod, A., Ecker, R., Ellinger, I., Luo, Z., Dong, B., Xu, Z., Yao, Y., Lv, S., Feng, M., Xu, K., Zunair, H., Hamza, A.B., Smiley, S., Yin, T.K., Fang, Q.R., Srivastava, S., Mahapatra, D., Trnavska, L., Zhang, H., Narayanan, P.L., Law, J., Yuan, Y., Tejomay, A., Mitkari, A., Koka, D., Ramachandra, V., Kini, L., Sethi, A., 2021. MoNuSAC2020: A multi-organ nuclei segmentation and classification challenge. *IEEE Trans. Med. Imaging* 40 (12), 3413–3423. <http://dx.doi.org/10.1109/TMI.2021.3085712>.
- Vu, Q.D., Kim, K., Kwak, J.T., 2020. Unsupervised tumor characterization via conditional generative adversarial networks. *IEEE J. Biomed. Health Inf.* 25 (2), 348–357.
- Wahab, N., Miligy, I.M., Dodd, K., Sahota, H., Toss, M., Lu, W., Jahanifar, M., Bilal, M., Graham, S., Park, Y., et al., 2021. Semantic annotation for computational pathology: Multidisciplinary experience and best practice recommendations. *J. Pathol. Clin. Res.*
- Wang, Y., Chao, W.L., Weinberger, K.Q., van der Maaten, L., 2019. SimpleShot: Revisiting nearest-neighbor classification for few-shot learning. arXiv preprint [arXiv:1911.04623](https://arxiv.org/abs/1911.04623).
- Zhang, R., Isola, P., Efros, A.A., 2016. Colorful image colorization. In: European Conference on Computer Vision. Springer, pp. 649–666.